

# *Herschel* and *Odin* observations of H<sub>2</sub>O, CO, CH, CH<sup>+</sup>, and [N II] in the barred spiral galaxy NGC 1365 ★ ★★

## Bar-induced activity in the outer and inner circumnuclear tori

Aa. Sandqvist<sup>1</sup>, Å. Hjalmarson<sup>2</sup>, B. Larsson<sup>1</sup>, U. Frisk<sup>3</sup>, S. Lundin<sup>4</sup>, and G. Rydbeck<sup>2</sup>

<sup>1</sup> Stockholm Observatory, Stockholm University, AlbaNova University Center, SE-106 91 Stockholm, Sweden  
e-mail: aage@astro.su.se

<sup>2</sup> Department of Space, Earth and Environment, Chalmers University of Technology, Onsala Space Observatory, SE-439 92 Onsala, Sweden

<sup>3</sup> Omnisys Instruments AB, Ringvägen 100E, SE-118 60 Stockholm, Sweden

<sup>4</sup> OHB Sweden, PO Box 1269, SE-164 29 Kista, Sweden

Received <8 July 2020>; accepted <22 December 2020>

### ABSTRACT

**Context.** The *Odin* satellite is now into its twentieth year of operation, much surpassing its design life of two years. One of its major astronomical pursuits was the search for and study of water vapor in diverse regions of the Solar System and the Milky Way galaxy. The *Herschel* space observatory was needed to detect water vapor in external galaxies.

**Aims.** Our goal is to study the distribution and excitation of water vapor and other molecules in the barred spiral galaxy NGC 1365.

**Methods.** *Herschel* has observed the central region of NGC 1365 in two positions, and both its SPIRE and PACS observations are available in the *Herschel* Science Archive. *Herschel* PACS images have been produced of the 70 and 160  $\mu\text{m}$  infrared emission from the whole galaxy, and also of the cold dust distribution as obtained from the ratio of the 160 to 70  $\mu\text{m}$  images. The *Herschel* SPIRE observations have been used to produce simultaneously observed maps of the 557 GHz o-H<sub>2</sub>O, 752 GHz p-H<sub>2</sub>O, 691 GHz CO(6–5), 1037 GHz CO(9–8), 537 GHz CH, 835 GHz CH<sup>+</sup>, and the 1461 GHz [N II] lines (efficiently probing the warm ionized medium) in the inner bar and circumnuclear torus region; – however, these observations have no effective velocity resolution. For this reason *Odin* has recently observed the 557 GHz ortho-H<sub>2</sub>O ground state line in the central region with high (5 km s<sup>-1</sup>) spectral resolution.

**Results.** The emission and absorption of H<sub>2</sub>O at 557 GHz, with a velocity resolution of 5 km s<sup>-1</sup>, has been marginally detected in NGC 1365 with *Odin*. The water vapor is predominantly located in a shocked 15'' (1.3 kpc) region near some central compact radio sources and hot-spot H II regions, close to the northeast component of the molecular torus surrounding the nucleus. An analysis of the H<sub>2</sub>O line intensities and velocities indicates that a shock-region is located here. This is corroborated by a statistical image deconvolution of our SEST CO(3–2) observations, yielding 5'' resolution, and a study of our Very Large Array (VLA) H I absorption observations, as well as comparisons with published interferometric CO observations. Additionally, an enticing 20'' H I ridge is found to extend south-southeast from the nucleus, coinciding in position with the southern edge of an O III outflow cone, emanating from the nucleus. The molecular chemistry of the shocked central region of NGC 1365 is analyzed with special emphasis on the CO, H<sub>2</sub>O and CH, CH<sup>+</sup> results.

**Conclusions.** The dominating activity near the northeast (NE) torus component may have been triggered by the rapid bar-driven inflow into the circumnuclear torus causing cloud-cloud collisions and shocks, leading to the formation of stellar superclusters and, hence, also to more efficient PDR chemistry, which, here, may also benefit from cosmic ray focusing caused by the observed aligned magnetic field. The very high activity near the NE torus component may reflect the fact that the eastern bar-driven gas inflow into the NE region is much more massive than the corresponding western gas inflow into the southwest (SW) region. The H<sub>2</sub>O and CH<sup>+</sup> emissions peak in the NE torus region, but the CO and CH emissions are more evenly distributed across the whole circumnuclear torus. The higher energy CO spectral line energy distribution (SLED) is nicely modeled by a low velocity (10 km s<sup>-1</sup>) shock, which may as well explain the required CH excitation and its high abundance in denser gas. The higher velocity (40 km s<sup>-1</sup>) shock required to model the H<sub>2</sub>O SLED in the NE torus region, paired with the intense UV radiation from the observed massive young stellar superclusters, may also explain the high abundance of CH<sup>+</sup> in this region. The nuclear H I ridge may have been created by the action of outflow-driving X-ray photons colliding with ice-covered dust grains. A precessing nuclear engine, as is suggested by the tilted massive inner gas torus, may be necessary to explain the various nuclear outflows encountered.

**Key words.** Galaxies: ISM – Galaxies: individual: NGC 1365 – Galaxies: Seyfert – Galaxies: nuclei

Send offprint requests to:

Aage Sandqvist, e-mail: aage@astro.su.se

\* *Herschel* is an ESA space observatory with science instruments provided by European-led Principal Investigator consortia and with important participation from NASA. *Herschel* was launched on May 14, 2009 and decommissioned on June 17, 2013.

\*\* *Odin* is a Swedish-led satellite project funded jointly by the Swedish National Space Board (SNSB), the Canadian Space Agency

(CSA), the National Technology Agency of Finland (Tekes), the Centre National d'Etudes Spatiales (CNES), France, and the European Space Agency (ESA). The former Space division of the Swedish Space Corporation, today OHB Sweden, is the prime contractor also responsible for *Odin* operations. *Odin* was launched on February 20, 2001 and is still in active operation.

## 1. Introduction

NGC 1365 is a prominent barred supergiant spiral galaxy in the Fornax cluster with a heliocentric velocity of  $+1632 \text{ km s}^{-1}$  (the velocity with respect to the Local Standard of Rest,  $V_{\text{LSR}} = 1613 \text{ km s}^{-1}$ , is used in this paper). In Fig. 1 we present a comparison of a visible-light “true-color” image of NGC 1365 from three exposures taken with the FORS1 camera on ESO’s VLT UT1, along with an infrared  $K$ -band image ( $0.9 - 2.5 \mu\text{m}$ ) obtained with the HAWK-I camera on the ESO VLT UT4 telescope (ESO/P. Grosböl). The infrared picture suggests a smaller stellar bar, or disk, within the radius of the Inner Lindblad Resonance (ILR) of  $30''$  (P.A.B. Lindblad et al. 1996) that is roughly perpendicular to the larger bar (as well as elongated along the line of nodes). Alonso-Herrero et al. (2012) performed a thorough study of the infrared spectrum ( $3.6 - 500 \mu\text{m}$ ) of the central region of NGC 1365 using the *Herschel* Photodetector Array Camera and Spectrometer (PACS) and Spectral Photometric Imaging REceiver (SPIRE), as well as *Gemini* and *Spitzer*. From the *Herschel* Science Archive, we retrieved their  $70$  and  $160 \mu\text{m}$  PACS observations of NGC 1365 and display  $70 \mu\text{m}$  and  $160 \mu\text{m}$  images in Fig. 1, where we also indicate the high- and low-frequency beams, respectively, of the SPIRE spectrometer observations presented in Sect. 2.1. The galaxy displays a wide range of phenomena indicating activity – including a Seyfert 1.5 type nucleus with strong, broad, and narrow  $H\alpha$  lines. Ionized outflows from the active galactic nucleus (AGN) with velocities up to a few hundred  $\text{km s}^{-1}$  have been observed (e.g., Venturi et al. 2018 and references therein). Kristen et al. (1997) used the Hubble Space Telescope to study the Seyfert nucleus and circumnuclear hot spots in NGC 1365 and found these hot spots to be resolved into a number of bright compact condensations, which they interpreted as super star clusters (SSC). The magnetic field in the central region has been mapped at the NRAO VLA with a resolution of  $9''$  by Beck et al. (2005). Jörsäter & van Moorsel (1995) used the NRAO VLA to map the  $\text{H I}$  emission distribution in the arms and the bar. In this paper, we present the  $\text{H I}$  absorption results in the galaxy’s central region, which were not discussed by them. A rapidly spinning supermassive black hole has been disclosed at the center of NGC 1365 by Risaliti et al. (2013). At an assumed distance of  $18.6 \text{ Mpc}$  (Madore et al. 1998),  $1''$  corresponds to  $90 \text{ pc}$ . For an extensive review of NGC 1365, see Lindblad (1999).

To set a solid background of observational knowledge, we now provide a rather detailed introductory review upon which the interpretation of our own observations can be based. In a flattened rotating proto-galaxy – very likely created in the potential well of a cosmological dark matter fluctuation (Persson et al. 2010) – there exist intrinsic instability modes such as spiral and bar instabilities, which may be triggered by encounters with nearby galaxies or by internal “noise” (e.g., P.O. Lindblad 1960; Lin & Shu 1964; Shu et al. 1973; Sundelius et al. 1987; Pfenniger & Norman 1990; P.A.B. Lindblad et al. 1996; P.O. Lindblad 1999; Pinol-Ferrer et al. 2012). Here the A. Toomre (1964) (in)stability criterion is a useful constraint.

Inside corotation, the bar pattern velocity is slower than the rotational motion of the gas. According to modeling and observations (e.g., P.A.B. Lindblad et al. 1996; P.O. Lindblad et al. 1996; P.O. Lindblad 1999; Sakamoto et al. 2007; Elmegreen et al. 2009), the gas catches up with the bar, and when leaving it on the front side of the bar experiences a strong shock with a drop of velocity of up to a few hundred  $\text{km s}^{-1}$ . This leads to an inflow of gas along the curved leading dust lanes of the bar (in the eastern bar estimated to be  $\approx 22 M_{\odot}/\text{year}$  at an inflow velocity

of  $\approx 80 \text{ km s}^{-1}$ ), creating a rather massive rotating torus inside the ILR. Here the orbit crowding is expected to cause multiple cloud-cloud collisions and shocks, leading to cloud coalescing into very massive ( $\approx 10^7 M_{\odot}$ ) cloud complexes, as well as to the subsequent birth of OB stars and massive (several  $\times 10^6 M_{\odot}$ ) stellar superclusters, as is observed in the outer NGC 1365 torus (Elmegreen et al. 2009; Galliano et al. 2012; Fazeli et al. 2019). The aforementioned expectations were based upon the fact that massive OB stars are born (mainly) in the spiral arms – where orbit crowding and density wave streaming is causing cloud-cloud collisions and shocks (cf. Roberts & Stewart 1987; Rydbeck et al. 1985; Aalto et al. 1999; Schinnerer et al. 2010) – as concluded from the Milky Way observational result, that the number of giant  $\text{H II}$  regions in a specified volume roughly scales as  $\langle n(\text{H}_2) \rangle^2$ , where  $\langle n(\text{H}_2) \rangle$  is the mean  $\text{H}_2$  density in the same volume (Scoville et al. 1986). The physical reason for the increased stellar formation activity is the increased external pressure created by the spiral arm molecular cloud collisions, triggering multiple massive gravitational collapses in these clouds, already residing in their low internal pressure (low temperature) virial equilibrium. This is a result of the efficient cooling provided by spectral line radiation from the interstellar molecules  $^{12}\text{CO}$ ,  $^{13}\text{CO}$ ,  $\text{H}_2\text{O}$ , and other species – (astro)chemistry (e.g., Irvine et al. 1987; van Dishoeck & Blake 1998; van Dishoeck et al. 2013) and (astro)physics in a necessary collaboration (Goldsmith & Langer 1978; Takahashi et al. 1985; Neufeld et al. 1995; see Hjalmarsen & Friberg 1988 for a discussion and additional references).

The very active starburst region in the central parts of the NGC 1365 bar has been studied in CO molecular lines at high resolutions: the  $J = 3 - 2$  CO line with  $5''$  effective resolution (Sandqvist 1999; this paper), and the  $J = 2 - 1$  lines of  $^{12}\text{CO}$ ,  $^{13}\text{CO}$ , and  $\text{C}^{18}\text{O}$  with  $2''$  resolution (Sakamoto et al. 2007). Sandqvist et al. (1995) performed VLA aperture synthesis observations of the radio emission from ionized gas, revealing a lower level circumnuclear ring of radius  $\approx 9''$  ( $\approx 800 \text{ pc}$ ), interspersed with compact radio sources, all of which have spectral indices indicating free-free emission from hot ionized gas, except one, called “F”, which has the spectral index characteristic of synchrotron radiation (see Table 2). They also mapped the distributions of the CO  $J = 1 - 0$  and  $2 - 1$  lines using the SEST (Swedish ESO Submillimeter Telescope, now “retired”). In the nuclear region, the envisioned synchrotron jet is enshrouded by a fan- or rather cone-shaped ionized gas outflow, revealed by its visual  $\text{O III}$  emission (Fig. 7(4) and Hjelm & Lindblad 1996, discussed in detail in the review paper by Lindblad 1999). More recently this kpc-size wide-angle outflow of ionized gases was studied in detail by Lena et al. (2016) and Venturi et al. (2018). Combes et al. (2019) present Atacama Large Millimeter/submillimeter Array (ALMA) observations of CO( $3 - 2$ ) with a resolution of  $0''.1$  in a sample of seven Seyfert/LINER galaxies which includes NGC 1365, where they estimate a central AGN (black hole) mass of  $4 \times 10^6 M_{\odot}$  by model fitting to the velocity field observed inside a radius of  $1''.4$ . It appears that the rotation axis of the inner nuclear torus has a position angle (P.A.) and inclination (Incl.) – (P.A.  $\approx 160^\circ \pm 10^\circ$ ; Incl.  $\approx 63^\circ \pm 10^\circ$ ) – which markedly deviates from the common rotation axis of the spiral arm disk, the bar, and the outer molecular gas torus of the galaxy (P.A.  $\approx 130^\circ$ ; Incl.  $\approx 50^\circ$ ). The orientation of the (symmetry) axes of the nuclear outflows (the wide-angle bi-conical ionized gas outflow, the synchrotron radiation radio jet, as well as the narrow CO outflow outlined in the present paper) all seem to be co-aligned with the galaxy rotation axis. The tilted rotation axis of the inner nuclear torus, or accretion disk, may suggest that we are witnessing the

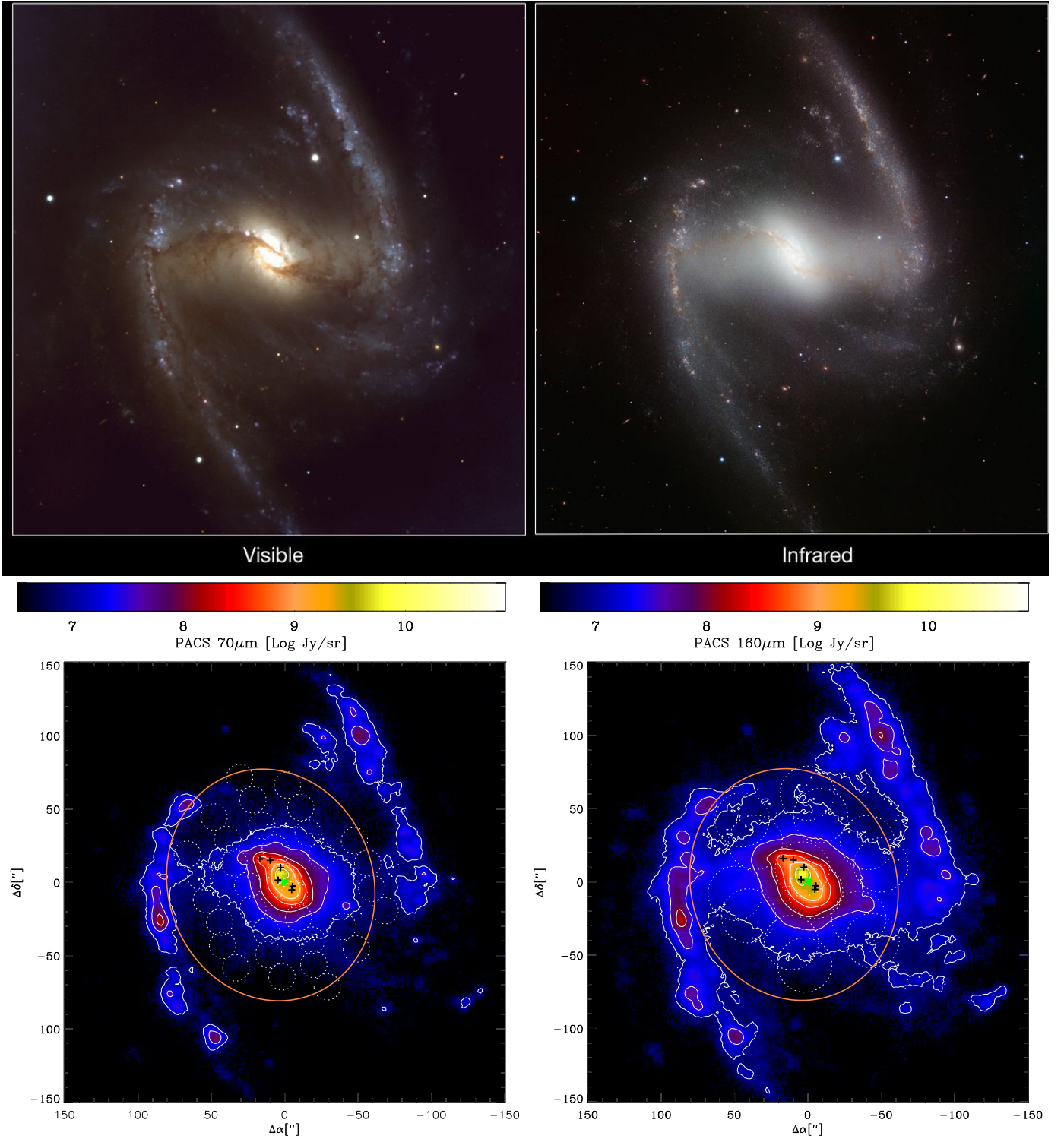


**Fig. 1.** *Top:* Visible-light “true-color” and infrared ( $0.9 - 2.5 \mu\text{m}$ ) images of NGC 1365, obtained with ESO’s VLT (ESO/P. Grosböl). *Bottom:* The  $70 \mu\text{m}$  and  $160 \mu\text{m}$  *Herschel* PACS images of NGC 1365 (beam sizes  $5''6$  and  $11''3$ ; Alonso-Herrero et al. 2012) on which are superimposed the high- and low-frequency beams ( $20''$  and  $40''$ , respectively, dashed circles) of the SPIRE spectrometer for the two sets of observations (toward the NE and SW positions, see Sect. 2.1) and the resultant beam ( $140'' \times 160''$ , solid ellipse) of the *Odin* observations. The crosses, from top to bottom (in decreasing declination), represent the “hot spot” H II regions L4, L11, L12, L1, L3, and L2 (Alloin et al. 1981). The equatorial offsets are with respect to the optical nucleus, which is marked with a green asterisk.

action of a precessing nuclear engine, a matter which will be outlined in our forthcoming discussion. The radius of the rotating inner torus, possibly a black hole accretion disk, was determined to be  $\approx 0.3''$  (26 pc) and its estimated gas mass is  $\approx 7 \times 10^6 M_{\odot}$ . Their larger scale mapping, in addition, confirms the outer ro-

tating circumnuclear molecular gas torus of radius  $9''$  (800 pc), already known from the  $\text{CO}(3 - 2)$  observations by Sandqvist (1999) and the  $\text{CO}(2 - 1)$  SubMillimeter Array (SMA) mapping by Sakamoto et al. (2007); compare also Fig. 7 of this paper.

The convincing signs of shocks in the NE outer torus region of NGC 1365 have indeed been observationally reported in terms of vibration-rotation  $2\ \mu\text{m}$   $\text{H}_2$  emission lines, requiring shock excitation and also pronounced Bry line wings, indicative of outflows and shocks emanating from three carefully studied superclusters (Galliano et al. 2012). Fazeli et al. (2019), in their recent VLT SINFONI near-IR observations of the central  $9'' \times 9''$  region of NGC 1365, found strong evidence of shocks – in terms of emission from several  $2\ \mu\text{m}$  vibration-rotation  $\text{H}_2$  lines, as well as from the “shock indicator line”  $\lambda 1.644\ \mu\text{m}$  “forbidden” Fe II – all emissions being strong in the SW and eastern side of the circumnuclear torus where the radio sources A, F, and H are situated (See Table 2). Source F may be especially interesting since it is the one being identified with the nuclear synchrotron radiation jet and CO outflow discussed in Sects. 4.3.1 and 4.3.2.

The outer much more massive torus is likely to be an important reservoir of matter, feeding the accretion disk of the supermassive black hole (SMBH), but the inward matter transport process between the outer and inner tori is still unclear. However, Lena et al. (2016), in their study of the nuclear outflow of ionized gas, also seem to “find kinematic components that may trace gas which has lost angular momentum and is slowly migrating toward the nucleus”. Here Fazeli et al. (2019) find “a spiral-shaped molecular gas structure (at a scale  $< 2''$ ) which could indicate inward streaming motions”. Such kinematic features also appear to be visible in the ALMA data of Combes et al. and hopefully will be discussed in their forthcoming study of gas outflow. Here the observed existence of a narrow relativistic plasma jet outflow and an accompanying co-aligned molecular gas outflow (jet) from the nuclear engine may be important. The cold gas expulsion process may be an upscaled version of the magneto-hydrodynamics (MHD) generation of the bi-polar outflows necessary to solve the angular momentum problem of star formation (e.g., Königl & Pudritz 2000; Arce et al. 2007), hence supporting the accretion toward the central AGN. The launching mechanism of the synchrotron jet as such may be a process closely connected with the angular momentum loss required for mass accretion onto and growth of the AGN (e.g., Blandford & Begelman 1999; Nayakshin 2014; Garcia-Burillo et al. 2014). For a more initiated and detailed discussion, we here refer to Aalto et al. (2016).

The submillimeter line spectrum of the Seyfert galaxy NGC 1068 has been observed with *Herschel* SPIRE by Spinoglio et al. (2012). While González-Alfonso et al. (2010, 2012) find that their *Herschel* SPIRE and PACS observations of multiple  $\text{H}_2\text{O}$  lines in the ULIRGs (Ultra-Luminous Infrared Galaxies) Mrk 231, NGC 4418, and Arp 220 were best modeled by FIR excitation (“radiation pumping”), the SPIRE observations of the early-stage merger galaxy NGC 6240 lead Meijerink et al. (2013) to conclude that shock excitation must be the cause of the CO-SLED (Spectral Line Energy Distribution). Submillimeter  $\text{H}_2\text{O}$  lines have been studied in detail in nine nuclei of actively star-forming galaxies using the *Herschel* HIFI, SPIRE, and PACS receivers (Liu et al. 2017). That sample did not include NGC 1365 but there are unpublished results which are available in the *Herschel* SPIRE and PACS Archive, and they form partial basis of the present paper. However, SPIRE does not yield spectral resolution capable of resolving any velocity structure across the galaxy in the signal. Since the 557 GHz (0.54 mm)  $\text{H}_2\text{O}$  line is a sensitive indicator of the existence of photodissociation regions (PDR) and other physical and chemical processes, leading to enhanced  $\text{H}_2\text{O}$  abundances such as outflows and shocks (e.g., Hjalmarsen et al. 2003, 2005; Gerin et al. 2016), we have used

the *Odin* satellite to probe the central region of NGC 1365 with high spectral resolution in this  $\text{H}_2\text{O}$  line.

The outline of this paper reads as follows. After an Introduction, containing a summary of the current knowledge of NGC 1365 relevant for the present communication, we present in Sect. 2 observations by the *Herschel* and *Odin* space telescopes. In Sect. 3 our new results from the *Herschel* PACS and SPIRE data and the complementary spectrally resolved *Odin* data are reported together with support analyses of SEST CO(3–2) and VLA H I data. In Sect. 4 our results concerning CO,  $\text{H}_2\text{O}$ , CH,  $\text{CH}^+$ , [N II], and H I are discussed in some detail. Our Summary and conclusions are provided in Sect. 5. For the interested reader, we have in Appendices B and C provided shortcut briefings on the interstellar chemistry of  $\text{H}_2\text{O}$  and CH,  $\text{CH}^+$  in prototype regions of our own Galaxy, wherein the physical and chemical conditions and processes are more accurately known, for comparison with observational results in external galaxies.

## 2. Observations

### 2.1. *Herschel* SPIRE

The nuclear region of NGC 1365 has been observed by *Herschel* using the SPIRE Fourier-transform spectrometer in the SpireSpectroPoint observing mode at two positions near the two maxima of the central CO torus, NGC 1365 NE: (J2000.0)  $3^{\text{h}}33^{\text{m}}36^{\text{s}}60, -36^{\circ}08'20''.0$  ( $+2''.8, +5''.4$ ), and NGC 1365 SW: (J2000.0)  $3^{\text{h}}33^{\text{m}}35^{\text{s}}90, -36^{\circ}08'35''.0$  ( $-5''.7, -9''.6$ ) – the numbers in parentheses are equatorial offsets from the optical nucleus. These observations, which are unpublished, were made on 22 August 2010 with total integration times of 3476 and 5640 seconds for the NE and SW positions, respectively. The channel resolution of the spectrometer is 1.447 GHz and the half-power beamwidth (HPBW) is roughly  $35''$  and  $20''$  for the low- and high-frequency parts of the spectra, respectively (Swinyard et al. 2010; cf. Fig. 1 of Spinoglio et al. 2012). We have retrieved these SPIRE observations from the *Herschel* Science Archive.

### 2.2. *Odin*

The observations of NGC 1365 in the 557 GHz  $\text{H}_2\text{O}$  line were performed with the *Odin* space telescope in December 2016, March and December 2017, and February 2018. The satellite was commanded toward the galaxy’s optical nucleus located at  $3^{\text{h}}33^{\text{m}}36^{\text{s}}37, -36^{\circ}08'25''.4$  (J2000.0) (Lindblad 1999). Position-switching was performed in right ascension with the OFF-position being displaced by  $-600''$ . The ON-source integration time was 7.4, 51.4, 14.5, and 10.9 hours in December 2016, March and December 2017, and February 2018, respectively. The backend spectrometer was a 1050-channel AOS with a channel resolution of 1 MHz. The system temperature was about 3500 K. The HPBW beamwidth of *Odin* at this frequency is 2:1 and the beam efficiency is 0.89 (Frisk et al. 2003). The nominal pointing accuracy of *Odin* is  $10''$ , but due to a systematic pointing error, slightly different positions were actually observed in the different periods. For the total averaged  $\text{H}_2\text{O}$  profile, this error led to an effective elliptical beam of  $140'' \times 160''$ , centered at an equatorial offset from the optical nucleus of ( $+10'', -2''$ ). This beam is also displayed in Fig. 1.

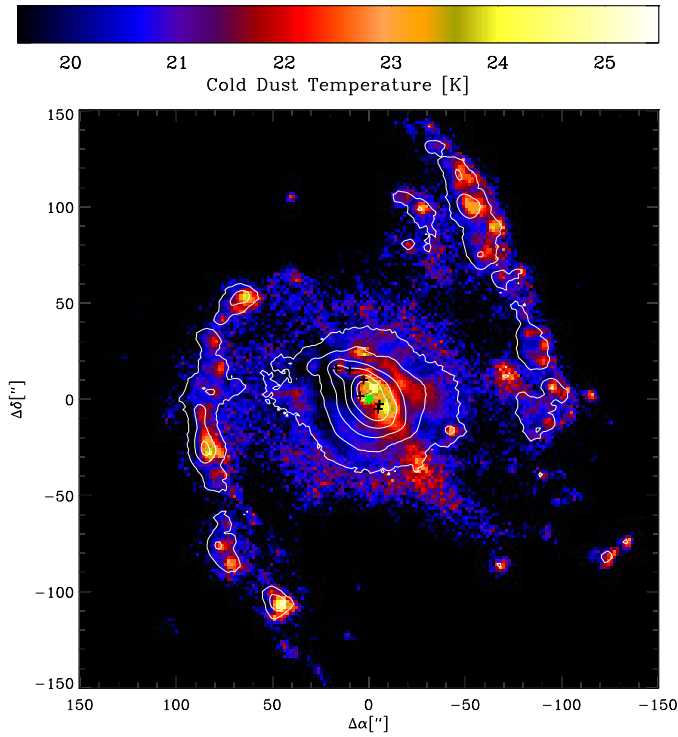


**Fig. 2.** Cold dust color temperature distribution in NGC 1365, obtained from the ratio of the 160  $\mu\text{m}$  to 70  $\mu\text{m}$  *Herschel* PACS images in Fig. 1. The contours indicate the 70  $\mu\text{m}$  intensities from Fig. 1. The crosses, from top to bottom (in decreasing declination), represent the “hot spot” H II regions L4, L11, L12, L1, L3, and L2. The equatorial offsets are with respect to the optical nucleus, which is marked with a green asterisk.

### 3. Results

#### 3.1. *Herschel* SPIRE and PACS results

From the ratio of the PACS 160  $\mu\text{m}$  to 70  $\mu\text{m}$  images of NGC 1365 presented in Fig. 1, we obtain a cold dust color temperature distribution for the entire galaxy (see Fig. 2) in a manner similar to Alonso-Herrero et al. (2012) who used the 100  $\mu\text{m}$  to 70  $\mu\text{m}$  PACS images for the central region.

The *Herschel* SPIRE apodized spectrum obtained toward the NGC 1365 NE torus position, corrected to a continuum source size of 14'' in a 40'' beam, is shown in Fig. 3. A myriad of lines has been detected for the following molecules: o-H<sub>2</sub>O and p-H<sub>2</sub>O, <sup>12</sup>CO, CH, NH, CH<sup>+</sup>, and atoms: [C I] and [N II]; their properties are listed in Table 1.

We have made map images of the combined NGC 1365 torus NE and SW *Herschel* SPIRE observations using the 557 GHz o-H<sub>2</sub>O and 752 GHz p-H<sub>2</sub>O lines, as well as the  $J = 6 - 5$  and  $9 - 8$  CO lines, 537 GHz CH and 835 GHz CH<sup>+</sup> lines. These images are shown in Fig. 4 where they are superimposed upon contours of the PACS 70  $\mu\text{m}$  observations (also seen in Fig. 1), which show the distribution of warm dust. We note that the NE torus region is much stronger in warm dust emission than the SW torus peak. The “hot spot” H II regions L1, L2, L3, L4, L11, and L12 (Alloin et al. 1981) are also indicated in these figures as is the position of the optical nucleus. Their equatorial offsets from the optical nucleus are listed in Table 2, as are the offsets of the compact radio sources detected by Sandqvist et al. (1995), and the co-located compact MidIR sources, detected and studied in detail by Galliano et al. (2005, 2008 and 2012) using adaptive optics on the ESO 3.6 m telescope and VLT. The co-location

**Table 1.** Parameters of the detected SPIRE spectral lines (Fig. 3), corrected to a continuum source size of 14'' in 40'' antenna beam

Species	Transition	Frequency [GHz]	$E_u$ [K]	Flux ( $10^{-17}$ W m <sup>-2</sup> )	Flux Error
<sup>12</sup> CO	J = 4-3	461.041	55.3	19.11	0.38
<sup>12</sup> CO	J = 5-4	576.268	83.0	19.27	0.38
<sup>12</sup> CO	J = 6-5	691.473	116.2	15.87	0.38
<sup>12</sup> CO	J = 7-6	806.652	154.9	11.95	0.38
<sup>12</sup> CO	J = 8-7	921.800	199.1	10.16	0.38
<sup>12</sup> CO	J = 9-8	1036.91	248.9	6.86	0.75
<sup>12</sup> CO	J = 10-9	1151.99	304.2	3.57 <sup>a</sup>	0.79
<sup>12</sup> CO	J = 11-10	1267.01	365.0	3.50	0.75
<sup>12</sup> CO	J = 12-11	1382.00	431.3	(1.85)	0.75
<sup>12</sup> CO	J = 13-12	1496.92	503.1		0.75
o-H <sub>2</sub> O	1 <sub>10</sub> -1 <sub>01</sub>	556.936	60.9	1.10	0.38
o-H <sub>2</sub> O	3 <sub>12</sub> -3 <sub>03</sub>	1097.36	249.4	2.88	0.75
o-H <sub>2</sub> O	3 <sub>12</sub> -2 <sub>21</sub>	1153.13	249.4	(1.18) <sup>a</sup>	0.79
o-H <sub>2</sub> O	3 <sub>21</sub> -3 <sub>12</sub>	1162.91	305.2	2.21	0.75
o-H <sub>2</sub> O	5 <sub>23</sub> -5 <sub>14</sub>	1410.62	642.4		0.75
p-H <sub>2</sub> O	2 <sub>11</sub> -2 <sub>02</sub>	752.033	136.9	1.49	0.38
p-H <sub>2</sub> O	4 <sub>22</sub> -3 <sub>31</sub>	916.172	454.3	(0.66)	0.38
p-H <sub>2</sub> O	2 <sub>02</sub> -1 <sub>11</sub>	987.927	100.8	3.27	0.75
p-H <sub>2</sub> O	1 <sub>11</sub> -0 <sub>00</sub>	1113.34	53.4	(0.92)	0.75
p-H <sub>2</sub> O	4 <sub>22</sub> -4 <sub>13</sub>	1207.64	454.3		0.75
p-H <sub>2</sub> O	2 <sub>20</sub> -2 <sub>11</sub>	1228.79	195.9	2.86	0.76
CH	1 <sub>3/2</sub> -1 <sub>1/2</sub>	532.7	25.7	1.19	0.38
CH	1 <sub>3/2</sub> -1 <sub>1/2</sub>	536.8	25.8	1.81	0.38
CH	2 <sub>3/2</sub> -1 <sub>3/2</sub>	1470.7	96.3	2.53	0.75
CH	2 <sub>3/2</sub> -1 <sub>3/2</sub>	1477.3	96.7	2.23	0.75
NH	1 <sub>2</sub> -0 <sub>1</sub>	974.48	46.8	2.82	0.76
NH	1 <sub>1</sub> -0 <sub>1</sub>	999.97	48.0	(1.06)	0.76
CH <sup>+</sup>	1-0	835.137	40.1	1.47	0.38
[C I]	<sup>3</sup> P <sub>1</sub> - <sup>3</sup> P <sub>0</sub>	492.161	23.6	9.06	0.38
[C I]	<sup>3</sup> P <sub>2</sub> - <sup>3</sup> P <sub>1</sub>	809.342	62.5	15.06	0.38
[N II]	<sup>3</sup> P <sub>1</sub> - <sup>3</sup> P <sub>0</sub>	1461.128	70.1	87.60	0.75

(<sup>a</sup>) Blended CO and H<sub>2</sub>O

with CO(2 – 1) intensity peaks in the 2'' resolution SMA aperture synthesis mapping by Sakamoto et al. (2007) is also convincingly illustrated in their Figs. 9 and 10, and is confirmed in the ALMA CO(3 – 2) higher resolution mapping by Combes et al. (2019).

The SEST maximum entropy method (MEM) map of the  $J = 3 - 2$  CO line with 5'' resolution (Sandqvist 1999) showed that a central molecular torus exists around the nucleus with the NE and SW peaks being of similar magnitudes. This is in clear contrast to the appearance of the 557 GHz o-H<sub>2</sub>O and 752 GHz p-H<sub>2</sub>O lines where the NE torus peak is considerably stronger than the SW peak, as can be seen in Fig. 4. This is also illustrated in Fig. 6 where the SPIRE profiles for these lines are presented. Since the torus peak positions NE and SW are separated by only 15'' while the beam size is 35'', Fig. 6 in fact tells us that the H<sub>2</sub>O emissions are very weak in the SW torus peak.

#### 3.2. *Odin* high spectral resolution H<sub>2</sub>O results

The *Odin* observations of NGC 1365 in the 557 GHz H<sub>2</sub>O line for the four different periods were integrated yielding a resultant profile with a total ON-source integration time of 81 hours. In Fig. 5 “Top”, we present the resultant profile with a channel resolution of 0.54 km s<sup>-1</sup> and a linear baseline subtracted. In the “Upper Middle” part of Fig. 5 we binned the *Odin* profile to a velocity resolution of 5 km s<sup>-1</sup> and compare it with several

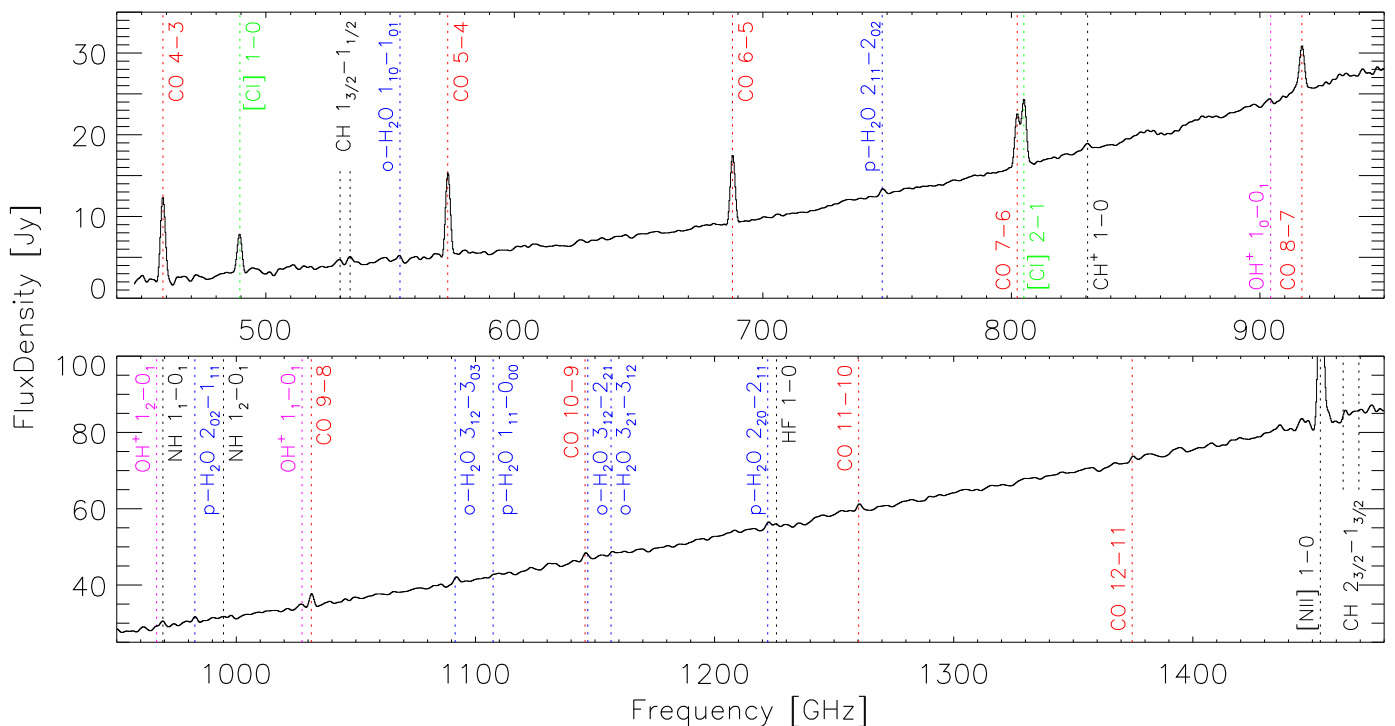


**Fig. 3.** *Herschel* SPIRE apodized spectrum toward NGC 1365 NE, corrected to a continuum source size of 14'' in a 40'' antenna beam. The abscissa is the observed frequency. Semi-extended source calibration is applied according to the SPIRE Handbook ([http://herschel.esac.esa.int/Docs/SPIRE/spire\\_handbook.pdf](http://herschel.esac.esa.int/Docs/SPIRE/spire_handbook.pdf)).

CO(3 – 2) profiles – from mapping observations obtained with SEST (Sandqvist 1999). The blue profile is the total SEST *Odin*-beam-convolved CO(3 – 2) profile. Two 5''-resolution SEST statistical image deconvolution (SID) CO(3 – 2) line profiles (see Sect. 3.4), observed close to the NE torus peak, are also presented in this panel. The green CO profile is in the direction of  $(\Delta\alpha, \Delta\delta) = (+6'', +8'')$ ; the red CO profile is in the direction of  $(\Delta\alpha, \Delta\delta) = (+7'', +3'')$ . In the “*Lower Middle*” panel of Fig. 5, we binned the *Odin* H<sub>2</sub>O profile to a velocity resolution of 30 km s<sup>-1</sup> and indicate the 1 $\sigma$  rms noise level of 0.9 mK as a red line. Two emission features are above the 3 $\sigma$  level, one near 1450 km s<sup>-1</sup>, the other near 1570 km s<sup>-1</sup>. There may also be an absorption feature with a 2 $\sigma$  intensity near 1500 km s<sup>-1</sup>. It is interesting that near these three velocities there exist corresponding CO(3 – 2) components in the green profile, presented in the *Upper Middle* panel of Fig. 5, a profile observed near the radio continuum source G (see Table 2). The intensity of the SPIRE data from Fig. 3, convolved to an *Odin* beam, has an intensity similar to the *Odin* data convolved to the 1.4 GHz SPIRE resolution. This is shown in Fig. 5 “*Bottom*” where these two profiles have been superimposed. From the evidence presented in Fig. 5, we draw the conclusion that *Odin* has indeed made a marginal detection of H<sub>2</sub>O in NGC 1365 – two H<sub>2</sub>O emission features near 1450 and 1570 km s<sup>-1</sup> and a possible absorption feature near 1500 km s<sup>-1</sup>.

### 3.3. VLA H<sub>I</sub> observations of the central regions of NGC 1365

We have used the VLA H<sub>I</sub> data cube of Jörsäter & van Moorsel (1995) to study the central region of NGC 1365 in greater detail, using both the emission and absorption data. The total integrated line intensity map is shown in Fig. 7. Emission is dominant at the H<sub>II</sub> region L4, absorption at the compact radio sources D, E and G, but a marked absorption also is seen at F. Four velocity-

integrated maps, spaced at 100 km s<sup>-1</sup>, are presented in Fig. 8. The dominant H<sub>I</sub> emission is in the (–228 to –104) km s<sup>-1</sup> velocity interval and originates in the L4 region at the upper left part of that figure near offsets (+17'', +16''). The major H<sub>I</sub> absorption is seen in the velocity interval (–104 to 0) km s<sup>-1</sup> and comes from the D, E, G region near offsets (+1'', +7''), as can be seen in Fig. 8. And, finally, Fig. 8 shows that the major absorption region in the velocity interval of (0 to +104) km s<sup>-1</sup> comes from the F region at offsets near (+3'', –3''), and in the velocity interval of (+104 to +228) km s<sup>-1</sup> comes from the region around sources A, L2 and L3, in the lower right of that H<sub>I</sub> figure. One may compare these features with the three velocity components seen in the *Odin* H<sub>2</sub>O profile presented in Fig. 5 “*Upper Middle*”, namely the two emission peaks near 1460 (–150) and 1560 (–50) km s<sup>-1</sup> and the absorption component at 1510 (–100) km s<sup>-1</sup>, where the velocities in brackets are relative to the systemic velocity, all three originating northeast of the nucleus. The H<sub>I</sub> position-velocity (P-V) maps are presented in Appendix A. In Fig. A.1 (for  $y = 0''$ ), the map is along the major axis of NGC 1365, through L4 (wide emission), G (strong absorption), the nucleus (empty), and finally A and L3 (absorption). The H<sub>I</sub> map in Fig. A.1 (for  $y = +2.5''$ ) is parallel to the major axis but 2''.5 southeast of it, thus passing through F – the absorption close to +50 km s<sup>-1</sup> appears at the position of F.

### 3.4. Statistical image deconvolution analysis of our $J = 3 - 2$ CO SEST observations

The SEST CO(3 – 2) observations of NGC 1365, published by Sandqvist (1999), were performed over an  $\approx 120'' \times 60''$  region centered on the optical nucleus. A grid spacing of 10'' was used for the outer parts of the region whereas a grid spacing of 5'' was used for the inner  $\approx 70'' \times 40''$  region. We have applied a statistical image deconvolution (SID) analysis (Rydbeck 2008)

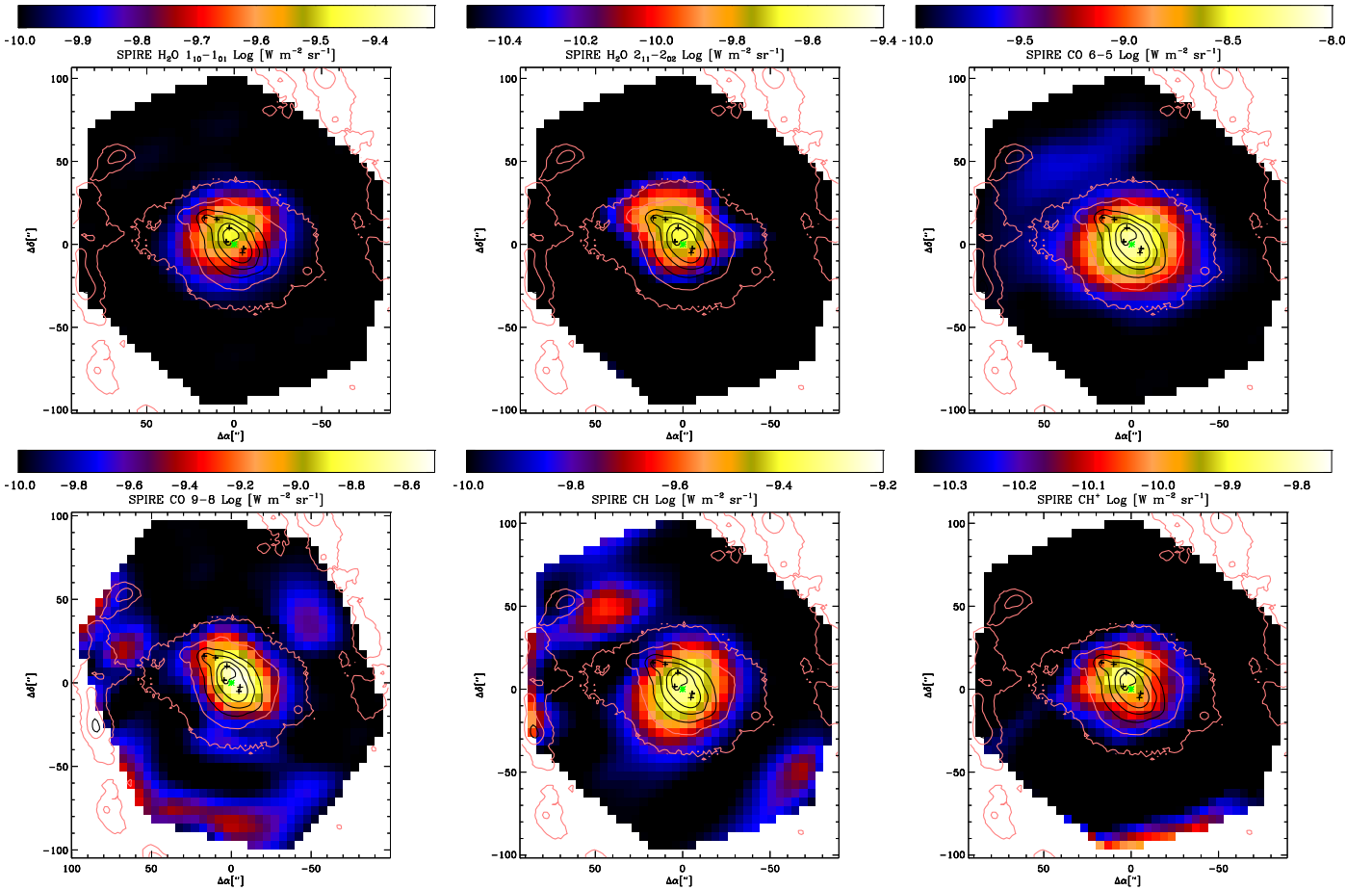


**Fig. 4.** SPIRE maps of 557 GHz o-H<sub>2</sub>O ( $\approx 35''$ ), 752 GHz p-H<sub>2</sub>O ( $\approx 35''$ ),  $J = 6 - 5$  CO ( $\approx 30''$ ),  $J = 9 - 8$  CO ( $\approx 20''$ ), 537 GHz CH ( $\approx 35''$ ), and 835 GHz CH<sup>+</sup> ( $\approx 35''$ ), the beamwidths are in parentheses. The contours are from the PACS 70  $\mu$ m observations seen in Fig. 1 and reflect the distribution of warm dust, the maximum being near the NE torus component. The crosses, from top to bottom (in decreasing declination), represent the “hot spot” H II regions L4, L11, L12, L1, L3, and L2, the latter two being near the SW torus component. The equatorial offsets are with respect to the optical nucleus which is marked with a green asterisk.

to the SEST  $J = 3 - 2$  CO observations to obtain high resolution ( $5''$ ) maps at different velocities and P-V maps. These maps will help us to identify the origins of the different *Odin* H<sub>2</sub>O components. The intensity unit in the maps is antenna temperature. The main beam efficiency of 0.26 has been applied in the P-V maps to yield main beam brightness temperature. Examples of CO integrated intensity maps for the total and selected velocity intervals are shown in Figs. 7 and 8; examples of CO P-V maps are shown in Fig. A.1.

A comparison of the integrated intensity H I absorption and CO emission maps, seen in Fig. 7, shows that the main features in both species are oriented in a northeast-southwest direction along the circumnuclear torus. There is an additional somewhat enticing feature seen in the H I map, namely, an approximately  $20''$ -long H I absorption ridge emanating from the nucleus in a south-southeast direction. This H I ridge may have a CO counterpart as shown by the low-level extension in the same direction in the CO map. A careful study of the H I and CO maps in Fig. 8 shows that this ridge has a very wide velocity dispersion. This ridge will be discussed further in Sect. 4.3.1.

## 4. Analysis and discussion

### 4.1. Gas distribution, dynamics, and star formation in the central region of NGC 1365

The distribution of molecular gas in the central region of NGC 1365 can be understood in the framework of bar-driven gas dynamics, as described in the Introduction. This implies that the rapid inward gas flows along the bar dust lanes are transferred into an oval circumnuclear torus of streaming gas clouds (see Sakamoto et al. 2007, especially their Fig.12).

#### 4.1.1. Cold molecular gas clouds causing intense star formation

According to our *Herschel* SPIRE mapping (Fig. 4), the ground state o-H<sub>2</sub>O ( $1_{10} - 1_{01}$ ) emission at 557 GHz, observed by *Odin* in NGC 1365 (in the velocity range  $1400 - 1650$  km s<sup>-1</sup>), is mainly emanating from within a  $10 - 15''$  size (i.e.,  $\approx 1$  kpc) region, including the NE hot spot (of CO, etc.) of the circumnuclear torus and some very nearby hot spots east thereof. However, we cannot exclude that some of the water emission in the velocity range  $1400 - 1500$  km s<sup>-1</sup> emanates from the L4 hot spot situated in the leading dust lane of the eastern bar, about  $25''$  away from the center (see e.g., Fig. 1), since this is also the velocity range observed at this position in the CO( $3 - 2$ ) line (see Fig. A.1).

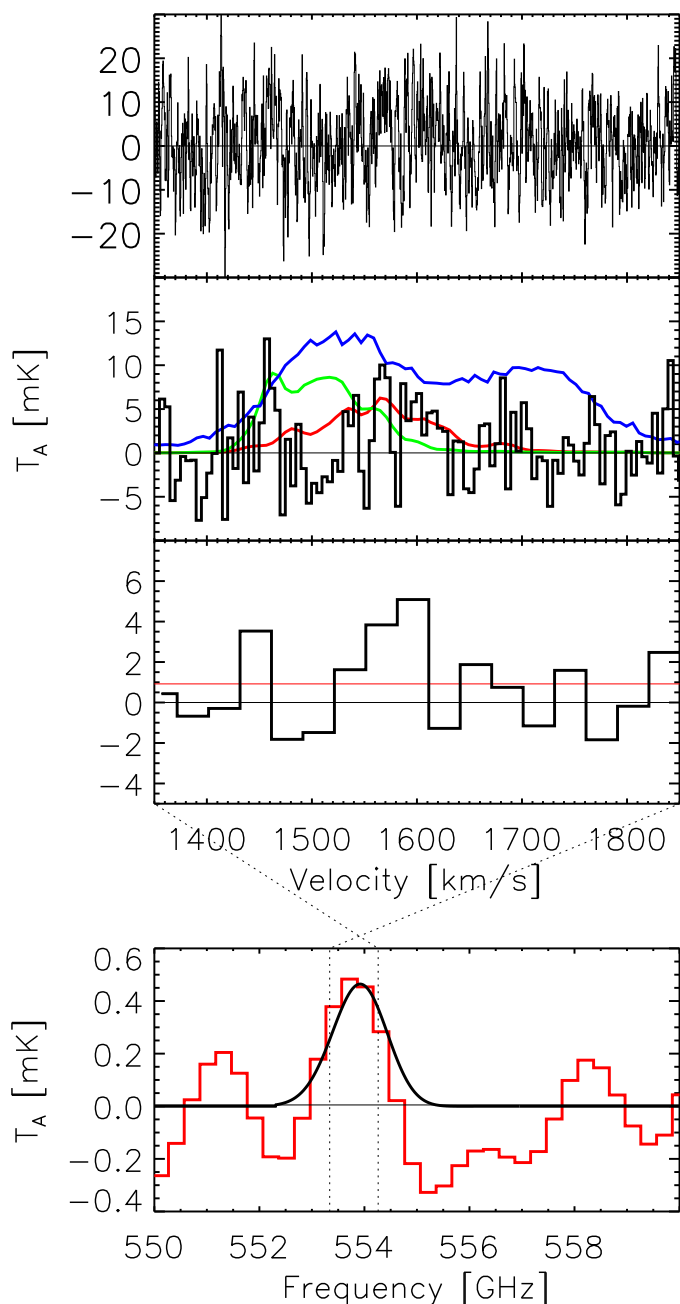


**Fig. 5.** *Odin* 557 GHz  $\text{H}_2\text{O}$  profile observed toward NGC 1365. *Top*: The unsmoothed profile with a resolution of  $0.54 \text{ km s}^{-1}$ . *Upper Middle*: The *Odin*  $\text{H}_2\text{O}$  profile binned to a resolution of  $5.0 \text{ km s}^{-1}$  (black); the SEST *Odin*-beam-convolved  $\text{CO}(3-2)$  profile (blue); the green and red SID CO profiles are observed near the NE torus component (Sect. 3.2). The CO profiles should be multiplied by a factor of 100. *Lower Middle*: The *Odin*  $\text{H}_2\text{O}$  profile binned to a resolution of  $30 \text{ km s}^{-1}$ . The  $1\sigma$  rms noise level of  $0.9 \text{ mK}$  is indicated in red. *Bottom*: The *Odin*  $\text{H}_2\text{O}$  profile convolved to a  $1.4 \text{ GHz}$  (SPIRE) resolution (black); the SPIRE data convolved to an *Odin*-beam resolution (red).

Our SPIRE map of the  $752 \text{ GHz}$  line in fact may support such a contribution, although not the  $557 \text{ GHz}$  line map (see Fig. 4).

It may seem peculiar that we observe little or no ground state  $\text{o-H}_2\text{O}$  emission from the SW torus region (i.e., in the velocity range  $1613 - 1800 \text{ km s}^{-1}$ ), since the  $\text{CO}(2-1)$  as well as the  $\text{CO}(3-2)$  emissions are observed to be similarly strong in the NE and SW torus regions (Sakamoto et al. 2007; Sandqvist

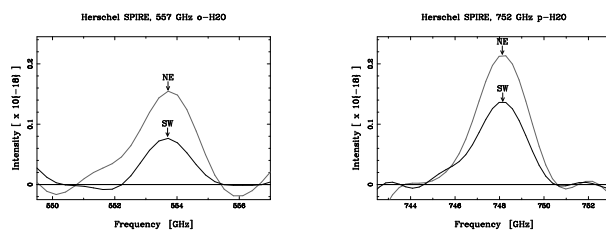


**Fig. 6.** *Herschel* SPIRE  $557\text{-GHz}$   $\text{o-H}_2\text{O}$  (left) and  $752\text{-GHz}$   $\text{p-H}_2\text{O}$  (right) profiles observed toward the NGC 1365 NE (gray) and SW (black) torus positions. Intensity units are  $\text{W m}^{-2} \text{ Hz}^{-1} \text{ sr}^{-1}$ . The HPBW beamwidth is  $35''$  and the separation between the NE and SW positions is  $15''$ .

**Table 2.** Equatorial offsets from the optical nucleus ( $3^{\text{h}}33^{\text{m}}36^{\text{s}}.37, -36^{\circ}08'25''.4$ ) of hot-spot  $\text{H II}$  regions (Alloin et al. 1981) and compact radio sources (Sandqvist et al. 1995).

Sources	$\Delta\text{RA}$ ( $''$ )	$\Delta\text{Dec}$ ( $''$ )	Line	Velocity (Width) <sup>a</sup> ( $\text{km s}^{-1}$ )
L4	+17	+16		
L11	+10	+15		
L12	+2	+11		
L1	+4	+2		
L3	-6	-3		
L2	-5	-5		
D (= M4)	0	+7	$\text{CO}(2-1)$	+1560 (70)
			Bry	+1555 (145)
			$\text{H}_2$	+1560 (?)
E (= M5)	+3	+10	$\text{CO}(2-1)$	+1540 (60)
			Bry	+1520 (145)
			$\text{H}_2$	+1530 (?)
G (= M6)	+5	+7	$\text{CO}(2-1)$	+1480 (80)
			Bry	+1475 (200)
			$\text{H}_2$	+1470 (?)
H (= M8?)	+5	+3	$\text{CO}(2-1)$	+1510 (70)
F <sup>b</sup>	+3	-3	$\text{CO}(2-1)$	+1590 (90)
A	-4	-3	$\text{CO}(2-1)$	$\approx 1730 - 1750$

(<sup>a</sup>) Velocities and line widths are from Sakamoto et al. (2007) and Galliano et al. (2012). (<sup>b</sup>) The steep spectrum of this compact radio source indicates emission from a synchrotron radiation outflow jet originating in the nuclear engine (Sandqvist et al. 1995; Lindblad 1999).

1999; Fig. A.1 of this paper). However, in addition to the lack of sensitivity in our *Odin* observations, a likely explanation is offered by the recent mapping of the dust emission at  $870 \mu\text{m}$  in NGC 1365 using LABOCA (the Large APEX Bolometer Camera; Tabatabaei et al. 2013). These authors estimate that the eastern bar is more massive than the western one by at least a factor of four. Hence the bar-driven inflow of gas into the NE torus region may be expected to be much more massive than the similar inflow into the SW torus region. Tabatabaei et al. also find that the dust (and presumably the gas) in the western bar is warmer (about  $40 \text{ K}$ ) than that in the eastern bar (about  $20 \text{ K}$ ) by a factor of two. Even the cold dust temperature map, presented in our Fig. 2, shows a tendency for the western bar to be warmer. This temperature difference may indeed explain why the (optically thick)  $\text{CO}(3-2)$  emissions remain similarly strong in the eastern and



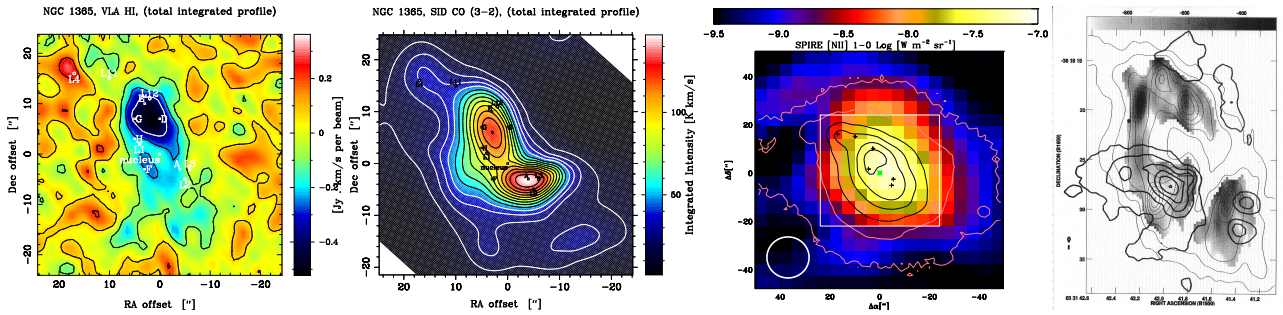


**Fig. 7.** Panel Number from the Left: (1): VLA H I line total integrated intensity distribution, emission and absorption, is shown in the central region of NGC 1365. The circles are hot-spot H II regions and the squares are compact radio sources as defined in Table 2. The offsets are with respect to the optical nucleus, which is marked by a square. (2): The SEST SID CO(3 – 2) total integrated line intensity (antenna temperature – multiply by 3.8 to obtain main beam brightness temperature). The equatorial offsets are with respect to the optical nucleus. (3): The SPIRE map of 1461 GHz N II; the beamwidth is  $\approx 17''$ . The white square marks the area covered in the H I and CO maps. Remaining features are as defined in Fig. 4. (4): The O III emission line region (thick lines), and the VLA 20-cm radio continuum emission (thin lines) from the radio jet and the radio continuum circumnuclear ring. The gray scales, ranging from  $-0.3$  (black) to  $-1.0$  (white), indicate the 6/20 cm radio spectral index. The cross marks the position of the optical nucleus (from Sandqvist et al. 1995).

western torus and bar regions (Fig. 8 [ $-102$  to  $0$  km s<sup>-1</sup>] and [ $+102$  to  $+228$  km s<sup>-1</sup>]) in spite of the apparently very different gas masses.

Using the careful SMA aperture synthesis CO (2-1) mapping at  $2''$  resolution by Sakamoto et al. (2007), Elmegreen et al. (2009) estimate that the gas inflow into the NE torus region has a velocity of  $\approx 80$  km s<sup>-1</sup> and an accretion rate of  $\approx 22$  M<sub>⊙</sub>/yr. They also estimate a star formation rate (SFR) of  $\approx 10$  M<sub>⊙</sub>/yr in the central, circumnuclear torus region (using the observed FIR luminosity). Tabatabaei et al. (2013) find an SFR of  $\approx 15$  M<sub>⊙</sub>/yr in the central  $80''$  region in a similar way. Based upon their CO mapping, Sakamoto et al. (2007) and Sandqvist (1999) estimated the observed central molecular cloud mass to be  $M_{\text{mol}}(R \leq 1 \text{ kpc}) \approx 1 \times 10^9$  M<sub>⊙</sub> and  $M_{\text{mol}}(R \leq 2 \text{ kpc}) \approx 5.4 \times 10^9$  M<sub>⊙</sub>, respectively, however relying on very different  $X_{\text{CO}}$ -factors,  $0.5 \times 10^{20}$  vs.  $2.3 \times 10^{20}$  (K km s<sup>-1</sup>)<sup>-1</sup>. If we instead use a common conversion value of  $1.2 \times 10^{20}$  cm<sup>-2</sup> (K km s<sup>-1</sup>)<sup>-1</sup> in both cases, as suggested by Tabatabaei et al., we arrive at  $M_{\text{mol}}(R \leq 1 \text{ kpc}) \approx 2.4 \times 10^9$  M<sub>⊙</sub> and  $M_{\text{mol}}(R \leq 2 \text{ kpc}) \approx 2.8 \times 10^9$  M<sub>⊙</sub> – mass estimates likely to be accurate to within a factor of two.

Our CO(3 – 2) P-V diagram (Fig. A.1 [ $y = -2.5''$ ]) nicely demonstrates an overall solid body rotation (i.e., a rotational velocity increasing linearly with the distance from the center) of the circumnuclear molecular cloud torus region inside  $R \leq 1$  kpc, but with considerable velocity dispersion caused by individual cloud motion, cloud-cloud collisions, shocks and outflows (also causing increased turbulence in the clouds). For  $R > 1$  kpc we observe the expected differential rotation. In fact, we may also (in Fig. A.1 [ $y = -2.5''$ ]) see a hint of the NE bar-driven inflow in terms of two velocity components (at  $-150$  and  $-110$  km s<sup>-1</sup>, at a major axis offset of  $+10''$ , or  $0.9$  kpc). Correcting for a galaxy inclination of  $40^\circ$ , this velocity difference becomes close to the aforementioned inflow velocity of  $80$  km s<sup>-1</sup>. The P-V diagram also allows us to calculate the dynamical mass  $M_{\text{dyn}}$  (of gas, stars plus central AGN) inside a specified radius (using the balance between the centrifugal force caused by rotation at a velocity  $V_{\text{rot}}(R_o)$  and the gravitational attraction of the mass inside  $R_o$  – valid in the low-order approximation of circular motion), namely,

$$M_{\text{dyn}}(R \leq R_o) = R_o \times V_{\text{rot}}^2(R_o)/G, \quad (1)$$

where  $G$  is the gravitation constant, which in more useful parameters can be rewritten

$$M_{\text{dyn}}(R \leq R_o) \approx 1.2 \times 10^{10} M_{\odot} \times R_o[\text{kpc}] \times (V_{\text{rot}}/230)^2. \quad (2)$$

From our P-V-diagrams (Fig. A.1), we may now estimate  $V_{\text{rot}} \approx 150$  km s<sup>-1</sup>/sin  $40^\circ = 233$  km s<sup>-1</sup> and  $V_{\text{rot}} \approx 200$  km s<sup>-1</sup>/sin  $40^\circ = 311$  km s<sup>-1</sup> at  $R_o = 1$  and  $2$  kpc, and hence calculate dynamical masses of  $1.2 \times 10^{10}$  M<sub>⊙</sub> and  $4.4 \times 10^{10}$  M<sub>⊙</sub>, respectively. Our previously observationally determined gas masses amount to about 20% of the dynamical masses in the center versus an average of 6% in the more extended region (including the center). Hence we may see a trend of increasing gas mass fraction toward the center, but not unexpectedly the stellar mass dominates.

#### 4.1.2. Warm ionized medium, created by the intense star formation

We now move from the discussion of the bar-driven, outer circumnuclear molecular gas torus, causing the formation of supermassive stellar clusters, to the creation of the warm ionized medium (WIM), the ISM component surrounding the molecular cloud ensemble and the stellar superclusters, which is caused by the intense UV radiation of the multitude of newly formed stars.

Nitrogen has a higher ionization potential (14.5 eV) than does Hydrogen (13.6 eV) and will stay atomic N where hydrogen is atomic H or molecular H<sub>2</sub>, and becomes ionized N<sup>+</sup> where hydrogen is almost completely ionized H<sup>+</sup>. The  $205 \mu\text{m}$  N II line is easily collisionally excited in warmer gas since its upper state energy is  $70$  K and its critical density is only  $44$  cm<sup>-3</sup>. Hence it is an excellent probe of the WIM, consisting of moderately dense H II regions and ionized boundary layers of clouds, that is to say, a useful measure of the star formation rate (SFR) (Langer et al. 2016; Zhao et al. 2016). Our SPIRE map of the  $205 \mu\text{m}$  N II line (Fig. 7), observed with a  $17''$  beam, shows that this emission is extended beyond the SW torus peak and here is as intense as in the NE peak. The high SFR observed also at and beyond the SW torus peak provides a nice explanation of the higher dust, gas temperature ( $40$  vs  $20$  K) and lower dust, gas mass (by a factor four) in the western bar region versus the eastern bar, as estimated by Tabatabaei et al. (2013). This observed mass and temperature asymmetry of the bar may be understood if the western bar region resides in a, somewhat later, high SFR stage, where

a larger amount of the star forming molecular clouds has been consumed and where the intense UV radiation from the newly formed stars has heated the dust.

## 4.2. Analysis of the *Odin* and *Herschel* SPIRE observations

### 4.2.1. *Odin* results

A Gaussian fit with two emission and one absorption components has been applied to the *Odin* H<sub>2</sub>O profile shown in Fig. 5. The values for  $T_A$ ,  $V$ , and  $\Delta V$  are 7.1 mK, 1456 km s<sup>-1</sup>, 42 km s<sup>-1</sup> and 5.1 mK, 1582 km s<sup>-1</sup>, 81 km s<sup>-1</sup> for the emission components and -1.5 mK, 1511 km s<sup>-1</sup>, 40 km s<sup>-1</sup> for the absorption component. The two emission features appear at velocity offsets of -157 and -31 km s<sup>-1</sup> with respect to the systemic LSR velocity of 1613 km s<sup>-1</sup>. The absorption feature has a velocity offset of -102 km s<sup>-1</sup>. Although the Gaussian fit may be somewhat uncertain – due to the very low signal-to-noise ratio, and since the lower excitation foreground H<sub>2</sub>O regions may absorb not only the thermal dust continuum but also some of the velocity ranges of the background H<sub>2</sub>O emission from higher excitation regions – it is worthwhile to use the velocity information in an attempt to determine the origin of the these three 557 GHz H<sub>2</sub>O regions. In the following, we use our own SEST SID CO(3 – 2) and VLA H I results as well as the CO(2 – 1) SMA observations by Sakamoto et al. (2007) and new ALMA observations of the CO(3 – 2) line by Combes et al. (2019).

While the large *Odin* beam is covering most of the bar, the H<sub>2</sub>O region has already been limited in extent to the central region by our SPIRE 557 GHz H<sub>2</sub>O map presented in Fig. 4. The H<sub>2</sub>O emission is dominant near the NE torus component where the aforementioned hot spot L-regions and compact radio sources gather.

Our CO(3 – 2) P-V map in Fig. A.1 ( $y = -2''.5$ ) shows a distinct feature at a velocity offset of -150 km s<sup>-1</sup>, which is close to one of the H<sub>2</sub>O emission features velocity of -157 km s<sup>-1</sup>. That occurs at a major axis offset  $x = 10''$ . This position is very close to the compact radio source G (see Table 2) and is also the region in the ALMA velocity map where the velocity offset is most negative, namely  $\approx -150$  km s<sup>-1</sup>. Near the position of E, the ALMA velocity offset is around -90 km s<sup>-1</sup>, which is comparable to the *Odin* H<sub>2</sub>O absorption feature value of -102 km s<sup>-1</sup>. Near D the ALMA velocity offset is closer to -50 km s<sup>-1</sup>, which can be compared to the *Odin* emission feature value of -31 km s<sup>-1</sup>. The VLA H I maps in Fig. 8 show major absorptions toward G and D in the velocity offset ranges of (-228 to -104) km s<sup>-1</sup> and (-104 to 0) km s<sup>-1</sup>, respectively, agreeing reasonably well with the above-mentioned comparisons. Our conclusion is thus that the three *Odin* H<sub>2</sub>O features originate in the NE shock region, giving rise to the violent star formation activity caused by the interactions of the  $x_1$ - and  $x_2$ -like streamlines in the inner bar and center, as proposed by Sakamoto et al. (2007).

An estimate of the expected background continuum antenna temperature, convolved to the *Odin* effective beam of 140'' by 160'', can be obtained from the *Herschel* SPIRE spectrum seen in Fig. 3. The flux density continuum level at 555 GHz is 4.5 Jy which converts to 1.5 mK antenna temperature, convolved to the *Odin* beam.

We now make an effort to estimate H<sub>2</sub>O abundances based upon our three-component Gaussian fit to the 557 GHz ground state o-H<sub>2</sub>O spectrum observed by *Odin*. The absorption feature around 1511 km s<sup>-1</sup> has a width  $\Delta V = 40$  km s<sup>-1</sup> and appears to be saturated since the absorption is similar to, or larger than, the continuum level determined from our *Herschel* SPIRE spectrum

(Fig. 3). A column density estimate for this lower density, lower excitation foreground gas, or rather a lower limit thereof, then may be obtained from the relation (derived by Karlsson et al. 2013),

$$N(\text{H}_2\text{O}) = 4/3 \times 4.89 \times 10^{12} \times \tau(\text{H}_2\text{O}) \times \Delta V, \quad (3)$$

where we assume an optical depth  $\tau \approx 2 - 3$  and an ortho-to-para ratio OPR = 3. The resulting total water column density becomes  $N(\text{H}_2\text{O}) \geq (5 - 8) \times 10^{14}$  cm<sup>-2</sup>. The corresponding H<sub>2</sub> column density, in front of the source(s) of the thermal dust continuum emission (and H<sub>2</sub>O emission) being absorbed, may be estimated from the visual extinctions of the mid/near IR (and radio) sources M4, M5 and M6 (see Table 2), from their observed Br $\gamma$ /Br $\alpha$  ratios, estimated to be  $A_v = 13.5, 3.2$  and 8.5 mag, respectively (Elmegreen et al. 2009). If we use an ‘‘average’’  $A_v \approx 10$  mag in the scaling relation found from observations by the Copernicus satellite (Bohlin et al. 1978), that is,

$$N(\text{H}_2)/A_v = 0.94 \times 10^{21} \text{ cm}^{-2}, \quad (4)$$

our estimate would be  $N(\text{H}_2) \approx 1 \times 10^{22}$  cm<sup>-2</sup>, with a considerable uncertainty range (for a discussion and references see e.g., Hjalmarsen and Friberg 1988). However, this value is in fact about half of the average total column density found from our SID CO(3 – 2) analysis (soon to be discussed), which is a useful criterion of correctness. Finally, the water abundance can be estimated to be  $X(\text{H}_2\text{O}) = N(\text{H}_2\text{O})/N(\text{H}_2) \geq 5 \times 10^{-8}$  – an abundance level which is well accommodated by PDR chemistry in lower density, translucent and diffuse regions (e.g., Hollenbach et al. 2009, 2012; see also our Tables 5 and B.1).

Our previous absorption line analysis must be considered comparatively accurate – since the method itself relies on the realistic assumption that the absorbing molecular population is mainly residing in the lowest possible energy state – although the optical depth of the 557 GHz o-H<sub>2</sub>O absorption tentatively observed by *Odin* is uncertain. In case of the two weak emission features apparent in the same *Odin* spectrum, the analysis uncertainty stems to a large extent from the relatively poor knowledge of sizes, densities, and temperatures of the emission regions, which by nature also are bound to be inhomogeneous. Their approximate sizes of  $\approx 10''$  are estimated from our SID CO(3 – 2) maps at 5'' resolution (for the relevant velocity ranges shown in Fig. 8) and the SMA CO(2 – 1) maps at 2'' resolution by Sakamoto et al. (2007). Guidance on temperatures and densities is drawn from the analysis of our multi-transition CO observations by SEST and *Herschel* SPIRE, presented in Sect. 4.2.2. Two-component fits to the CO rotation diagram, as well as the CO SLED, reveal a hot ( $T_{\text{kin}} \approx 350$  K) component, most likely caused by shock excitation, together with a lukewarm ( $T_{\text{kin}} \approx 40$  K) component having an average H<sub>2</sub> density of  $10^4$  cm<sup>-3</sup>. The average H<sub>2</sub> column density of the latter component is estimated to be  $6.3 \times 10^{21}$  cm<sup>-2</sup> across a  $10'' \times 30''$  region. According to Eq. (4) this corresponds to a visual extinction  $A_v \approx 7$  mag. However, the surface filling factor of CO emission in this region may be less than 100%. The characteristics of this lukewarm region are very similar to what is expected from PDR-models for high FUV illumination (such as that in the Orion molecular cloud; cf. Fig. 7 of Hollenbach et al. 2009). This interpretation is also supported by the best two-component fit of the SED of the thermal dust emission from the central regions of NGC 1365 – one component at  $25 \pm 2$  K and a necessary second one at  $55 \pm 5$  K,

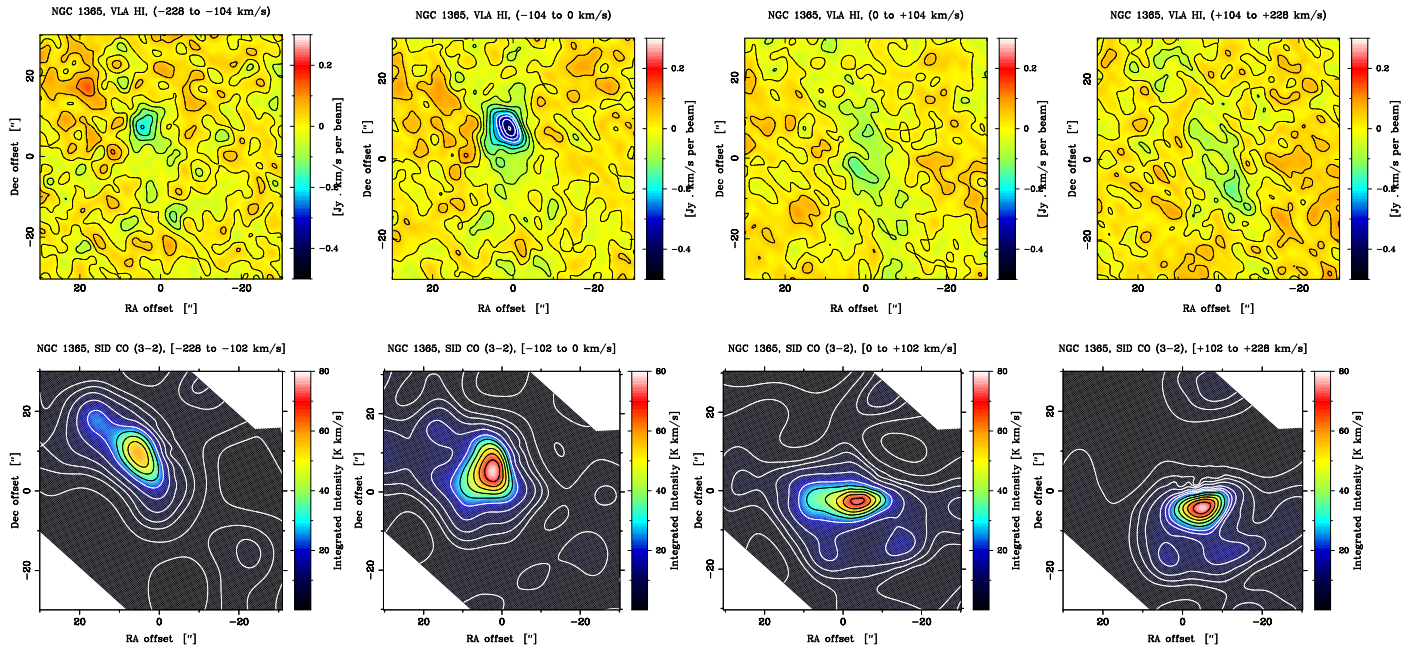


**Fig. 8.** VLA H I [*top*] and SEST SID CO(3 – 2) [*bottom*] line intensity maps integrated over the velocity range indicated in the header [–228 to –102], (–102 to 0), (0 to +102), (+102 to +228)] km s<sup>–1</sup>. The CO integrated intensity is antenna temperature – multiply by 3.8 to obtain main beam brightness temperature. The equatorial offsets are with respect to the optical nucleus. The velocity offsets are with respect to the systemic LSR velocity of 1613 km s<sup>–1</sup>.

emitted from  $\approx 1\%$  of the total dust mass (Alonso-Herrero et al. 2012; Tabatabaei et al. 2013).

With this information at hand, we assume a cloud temperature  $T_{\text{kin}} = 55$  K and density  $n(\text{H}_2) = 10^4 - 10^5$  cm<sup>–3</sup> in our RADEX (van der Tak et al. 2007) molecular excitation and radiative transfer model fitting of the 557 GHz o-H<sub>2</sub>O emission features, each having an estimated size of only  $\approx 10''$  in the very large *Odin* antenna beam ( $140'' \times 160''$ , resulting in a beam filling factor of 1/225). Including the beam filling correction, we get as input parameters  $T_b \approx 1.6$  K and  $\Delta V = 42$  km s<sup>–1</sup> for the emission around  $-157$  km s<sup>–1</sup> and  $T_b \approx 1.1$  K and  $\Delta V = 81$  km s<sup>–1</sup> for the emission around  $-31$  km s<sup>–1</sup>. If we assume an OPR = 3, the corresponding total ortho- and para-H<sub>2</sub>O column densities are RADEX modeled to be  $N(\text{H}_2\text{O}) \approx 15 \times 10^{15}$  cm<sup>–2</sup> and  $19 \times 10^{15}$  cm<sup>–2</sup>, respectively, for  $n(\text{H}_2) = 10^5$  cm<sup>–3</sup>, and increasing by an order of magnitude for the lower cloud density of  $n(\text{H}_2) = 10^4$  cm<sup>–3</sup>. The comparison H<sub>2</sub> column densities may be roughly estimated from our SID CO(3 – 2) maps for the velocity ranges  $-200$  to  $-100$  km s<sup>–1</sup> and  $-100$  to  $0$  km s<sup>–1</sup> (Fig. 8) using the scaling relation

$$N(\text{H}_2) = 1.2 \times 10^{20} \times I(\text{CO}) \text{ cm}^{-2}, \quad (5)$$

where  $I(\text{CO})$  is the integrated intensity [in K km s<sup>–1</sup>] (Tabatabaei et al. 2013; for a discussion of the scaling relation method, see e.g., Hjalmarsen & Friberg 1988), resulting in  $N(\text{H}_2) \approx 2.3 \times 10^{22}$  cm<sup>–2</sup> and  $3.0 \times 10^{22}$  cm<sup>–2</sup>, respectively, for the two H<sub>2</sub>O emission regions. For an average cloud density of  $10^5$  cm<sup>–3</sup>, the resulting H<sub>2</sub>O abundance versus H<sub>2</sub> can be calculated as  $X(\text{H}_2\text{O}) = N(\text{H}_2\text{O})/N(\text{H}_2) \approx 6 \times 10^{-7}$  for both regions – an abundance increasing by an order of magnitude in case the average density is  $10^4$  cm<sup>–3</sup>. The lower abundance value appears to be consistent with PDR modeling results (Hollenbach et al. 2009, 2012), especially since additional ionization support may exist in terms of cosmic ray focusing by the observed magnetic field alignment (Beck et al. 2005). However, substantial contri-

butions to the ground state H<sub>2</sub>O emission, caused by shock excitation and shock chemistry, are also expected from our modeling of the *Herschel* SPIRE data presented in Sect. 4.2.2 (see Fig. 9).

#### 4.2.2. *Herschel* SPIRE results

Before entering a detailed presentation of the multi-transition excitation and radiative transfer analysis of our SPIRE CO and H<sub>2</sub>O observations (Fig. 3 and Table 1), it may be helpful to examine the spatial distributions of the 557 GHz ground state o-H<sub>2</sub>O line ( $E_u = 27$  K in the ortho ladder;  $E_u = 61$  K vs the para ground state) and the 752 GHz excited state p-H<sub>2</sub>O line ( $E_u = 137$  K vs the para ground state), illustrated in Figs. 4 and 6. The two maps show that both lines are strongest in the NE torus peak area. However, it is apparent from Fig. 6 that the 557 GHz line has little or no emission at the SW torus peak, while the 752 GHz excited state transition definitely exhibits emission here (taking into account the beam size of  $35''$  and the  $15''$  separation of the observed NE and SW positions). Our subsequent analysis of the CO, as well as the H<sub>2</sub>O SLEDs, will lead us to the conclusion that shock excitation and shock chemistry must be main players in case of the higher energy lines. Therefore, it is useful to know beforehand that such conditions have indeed been observed in all of the “hot spot” H II, CO and stellar supercluster regions in the circumnuclear torus, and also in the presumptive synchrotron radiation jet source “F” (see our Table 2; VLT SINFONI high resolution near IR observations by Galliano et al. 2012 and Fazeli et al. 2019, to be discussed in some detail in Sect. 4.4).

We now present an analysis of the *Herschel* SPIRE apodized spectrum obtained toward the NE component of the central torus, which was presented in Fig. 3. As has already been pointed out, the NE component is the dominant one and so of major interest. It is also the component having a velocity field closer to that implied by the *Odin* H<sub>2</sub>O profile. We shall first treat the CO lines and then the H<sub>2</sub>O lines.

The rotation diagram for the CO lines is presented in Fig. 9(*Upper left*). The three lowest-level CO lines (blue dots) are obtained from SEST observations presented by Sandqvist et al. (1995), Sandqvist (1999), and Curran et al. (2001), while the remaining higher-level CO lines (red dots) are from this paper. The results of RADEX analysis applied to these CO lines (also presented in Fig. 9(*Upper left*)) show that the high  $J$  CO lines can be best fit by a single kinetic temperature of 400 K and an  $H_2$  density of  $n(H_2) = 3 \times 10^3 \text{ cm}^{-3}$ , yielding a CO column density of  $N(CO) = 2.5 \times 10^{15} \text{ cm}^{-2}$ .

A two-temperature RADEX fit to the CO SLED is presented in Fig. 9(*Upper right*). The best fit is obtained for an extended cold component with a temperature of  $T_{\text{Ext}} = 26 \text{ K}$ , density  $n(H_2) = 7 \times 10^3 \text{ cm}^{-3}$ , yielding a CO column density of  $N(CO) = 1 \times 10^{17} \text{ cm}^{-2}$ , and a hot component from a more compact region having a temperature of  $T_{\text{Hot}} = 350 \text{ K}$ , density  $n(H_2) = 10^4 \text{ cm}^{-3}$ , yielding a CO column density of  $N(CO) = 4 \times 10^{15} \text{ cm}^{-2}$ .

Perhaps it would be more realistic to study the NE region as one involving shocks (see Fig. 9(*Lower left*)). In this case we have used the C-shock model of Flower & Pineau des Forêts (2010) where we have scaled their values to an equivalent (accumulated) source size of  $10''$  in order to obtain a best fit. For the low  $J$  CO lines, we obtain here a slightly warmer extended region with a temperature of  $T_{\text{Ext}} = 40 \text{ K}$  and RADEX values of  $n(H_2) = 10^4 \text{ cm}^{-3}$  and  $N(CO) = 7 \times 10^{16} \text{ cm}^{-2}$  (represented by the blue curve) and a slow velocity C-type shock with a shock speed of  $10 \text{ km s}^{-1}$  and a pre-shock density of  $n(H+2H_2) = 2 \times 10^4 \text{ cm}^{-3}$  (represented by the red curve). This model yields a CO abundance of  $X(CO) \approx 10^{-4}$ .

Our RADEX modeling fit to the intensities of the lower energy lines yields  $N(CO) = 1 \times 10^{17} \text{ cm}^{-2}$  for a homogeneous cloud at a temperature  $T_{\text{kin}} \approx 40 \text{ K}$  and density  $n(H_2) = 10^4 \text{ cm}^{-3}$ . From the mapping of the CO(2–1) emission by Sakamoto et al. (2007) and our SID CO(3–2) deconvolution, it appears that the half power size of the emission region is only about  $30'' \times 10''$ , which means a beam filling of only 16% in a  $40''$  beam-size. The resulting CO column density hence becomes  $6.3 \times 10^{17} \text{ cm}^{-2}$ , which for a CO/ $H_2$  abundance ratio of  $\approx 1 \times 10^{-4}$  means an  $H_2$  column density  $\approx 6.3 \times 10^{21} \text{ cm}^{-2}$ . According to the scaling relation shown in Eq. (4), this corresponds to a visual extinction of  $\approx 7$  magnitudes. The estimated temperature and density, combined with this visual extinction, most likely tells us (cf. Hollenbach et al. 2009, 2012) that this CO emission must originate in the extended PDR surfaces of the molecular complexes, created by the intense UV illumination from the observed, co-located, newly formed, massive stellar superclusters (Elmegreen et al. 2009; Galliano et al. 2012; Fazeli et al. 2019).

We now turn our attention to the ortho- and para- $H_2O$  lines in the SPIRE spectrum of Fig. 3. RADEX models were performed for two different temperatures, namely 400 and 1000 K, and model values for density  $n(H_2) \text{ cm}^{-3}$  – and column density  $N(H_2O) \text{ cm}^{-2}$ , respectively, were  $10^3 - 3 \times 10^{14}$ ,  $10^4 - 3 \times 10^{13}$ ,  $10^5 - 3 \times 10^{12}$  for o- $H_2O$ ;  $10^3 - 10^{14}$ ,  $10^4 - 10^{13}$ ,  $10^5 - 10^{12}$  for p- $H_2O$ . None of these models were found to be applicable to the SPIRE  $H_2O$  data.

We then attempted water line modeling, using the same slow-velocity C-type shock as above in the CO line analysis, and these results are shown in Fig. 9(*Lower right*). In this figure the blue and red points and curves represent o- $H_2O$  and p- $H_2O$ , respectively. The ortho-to-para ratio is assumed to be 3. A shock speed of  $10 \text{ km s}^{-1}$  and a pre-shock density  $n(H_2) = 10^4 \text{ cm}^{-3}$ , nicely matching the SPIRE CO data, do not at all produce a fit to the observed  $H_2O$  lines. An improvement of the fit is obtained by

increasing the pre-shock density by an order of magnitude to  $n(H+2H_2) = 2 \times 10^5 \text{ cm}^{-3}$  and retaining the same shock speed of  $10 \text{ km s}^{-1}$ . But the best fit is obtained by using the original pre-shock density of  $n(H+2H_2) = 2 \times 10^4 \text{ cm}^{-3}$  and increasing the shock speed to  $40 \text{ km s}^{-1}$ . It is, however, still somewhat difficult to fit all the para- $H_2O$  lines. An approximate  $H_2O$  abundance for this model is similar to the CO abundance, that is to say,  $X(H_2O) = X(CO) \approx 10^{-4}$ . In studies of the SPIRE and PACS results for the ULIRGs Mrk 231, NGC 4418, and Arp 220, it has been found that FIR pumping provides an excellent fit to the observed  $H_2O$  line intensities (Gonzalez-Alfonso et al. 2010, 2012, 2014; cf. Yang et al. 2013). The estimated high  $H_2O$  abundances of  $10^{-6} - 10^{-5}$  here were suggested to result from shock chemistry, (multiple) hot cores, cosmic ray enhancement, XDRs, and, or “undepleted chemistry” where the icy grain mantles were evaporated. In our case of NGC 1365 FIR pumping, paired with an enhanced  $H_2O$  abundance caused by slow velocity shock sputtering of icy grain mantles (supplemented by any of the above processes), – all expected from observational data – this provides a viable alternative to “our poor man” fast shock modeling. Although no PACS observations of FIR pumping  $H_2O$  absorption lines are available in case of NGC 1365, we note that the observed intensity of the o- $H_2O$  ( $3_{21} - 3_{12}$ ) line, having an upper state energy of 305 K, is much higher than can be reached by the shock modeling (see Fig. 9(*Lower right*)). This strongly suggests that we see the effect of FIR pumping by o- $H_2O$  ( $2_{12} - 3_{21}$ ) absorption at  $75 \mu\text{m}$  (Gonzalez-Alfonso et al. 2014).

#### 4.3. Nuclear gas accretion and outflows

The gas inflow processes from the outer torus region onto the inner torus, nuclear accretion disk, of NGC 1365 were discussed already in the Introduction of this paper. We have in Table 3 collected a number of relevant parameters for the galaxy spiral arm disk, the bar, the bar-driven outer torus region, the inner cold gas torus, the central rapidly spinning SMBH, and the various observed nuclear outflows. We have also included in Table 3 some useful comparison parameters for the lens-shaped spiral galaxy NGC 1377, seen edge on, where rather convincing signs of a precessing nuclear bi-polar molecular outflow were observed at ALMA (Aalto et al. 2016).

##### 4.3.1. Atomic, molecular and ionic outflows, and a synchrotron radiation jet from the nuclear engine

It was mentioned already in the Introduction, that among the radio hot spots of the circumnuclear ring of gas in NGC 1365, ionized by recent star formation, the outer torus of radius 800 pc, a region “F” with a very steep radio spectrum was “hiding”, see Fig. 7(4) (Sandqvist et al. 1995). This was further illustrated in our Table 2. The envisioned synchrotron radiation relativistic outflow jet from, and presumably powered by, the nuclear engine, the black hole and its accretion disk, therefore is expected to be oriented along the rotation axis of the inner circumnuclear molecular gas torus. However, the projected jet orientation instead appears to be along the similar rotation axes of the galaxy, its prominent bar, and the outer molecular gas torus, and along the symmetry axis of the wide-angle ionized gas outflow observed in optical O III lines, as illustrated in Fig. 7(4) (Sandqvist et al. 1995; Hjelm & Lindblad 1996; Sandqvist 1999; Lindblad 1999; Venturi et al. 2018; see our Table 3). This observational fact is very important in our forthcoming scenario interpretation (Sect. 4.3.2). The observation of a synchrotron ra-

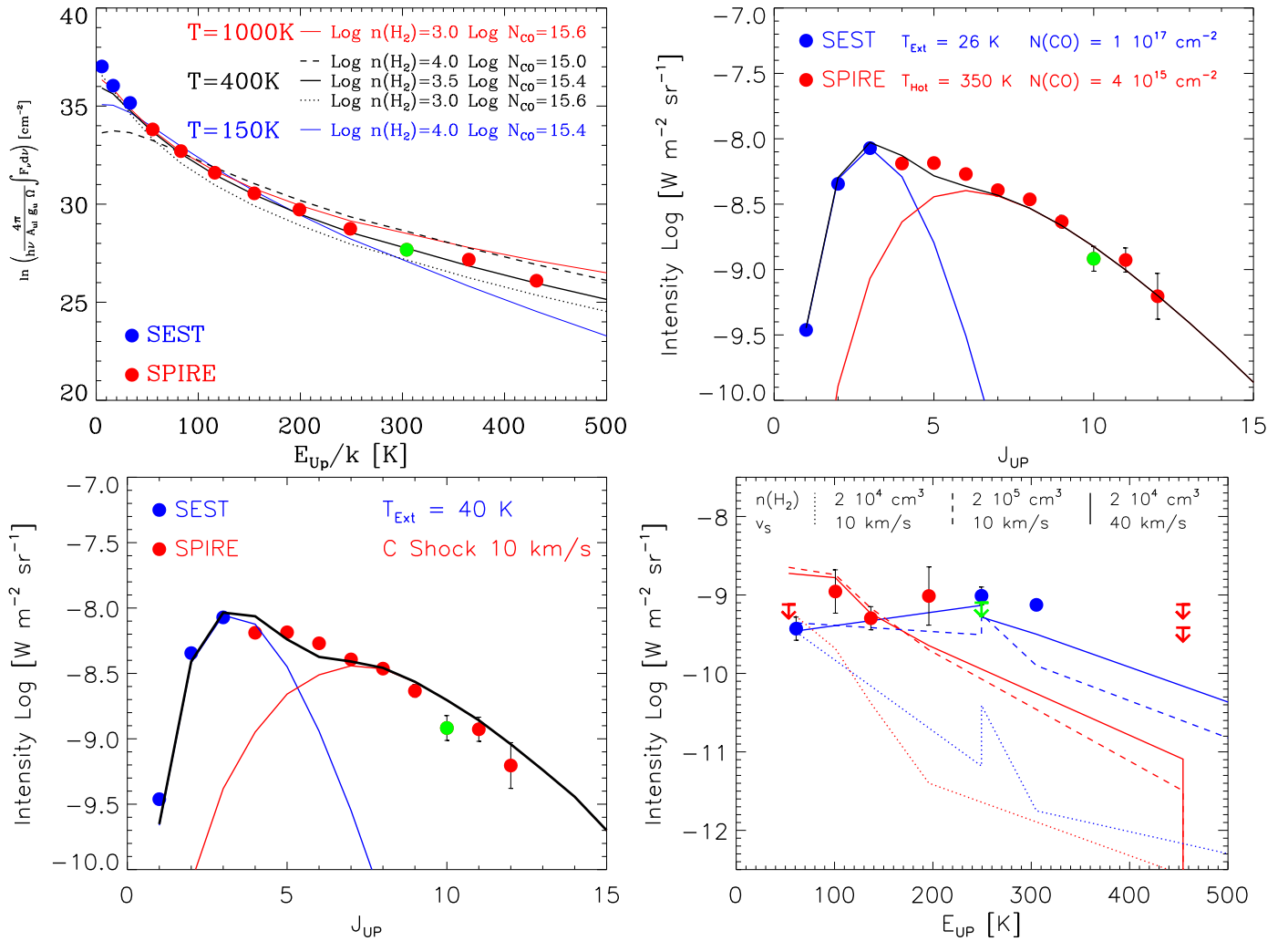


**Fig. 9.** *Upper left:* Rotation diagram for the CO lines. Blue dots: SEST observations from the literature, Red dots: SPIRE data, Green dot: SPIRE CO line blended with a water line. The full, dashed, and dotted lines show different single temperature RADEX models. *Upper right:* Two temperature (RADEX) fits to the CO lines. One extended cold component (blue) with  $n(\text{H}_2) = 7 \times 10^3 \text{ cm}^{-3}$  and  $N(\text{CO}) = 1 \times 10^{17} \text{ cm}^{-2}$ , and one hot component (red) from more compact regions  $n(\text{H}_2) = 10^4 \text{ cm}^{-3}$  and  $N(\text{CO}) = 4 \times 10^{15} \text{ cm}^{-2}$ . *Lower left:* A model consisting of a slightly warmer extended component with RADEX values of  $n(\text{H}_2) = 7 \times 10^3 \text{ cm}^{-3}$  and  $N(\text{CO}) = 7 \times 10^{16} \text{ cm}^{-2}$  (blue), and a slow velocity C-type shock with a shock speed of  $10 \text{ km s}^{-1}$  and a pre-shock density of  $n(\text{H} + 2\text{H}_2) = 2 \times 10^4 \text{ cm}^{-3}$  (red). The C-shock model comes from Flower & Pineau des Forêts (2010) where we have scaled their values to a  $10''$ -source in order to obtain a best fit. *Lower right:* Water lines modeling. Water emission lines observed by SPIRE – Blue dots: o-H<sub>2</sub>O, Green arrow: Blended ortho-line, Red dots: p-H<sub>2</sub>O. The same slow-velocity C-type shock as for CO but the model with a shock velocity of  $10 \text{ km s}^{-1}$  and a pre-shock density of  $n(\text{H} + 2\text{H}_2) = 2 \times 10^4 \text{ cm}^{-3}$  underestimates the line intensities. Increasing the speed or the pre-shock density will give a better fit but it’s still hard to fit all para lines.

radiation jet, having a de-projected size of some 400 pc, depending upon its somewhat uncertain inclination, see Table 3, in fact means that we are probing the radiative acceleration losses in a plasma beam where the electrons are spiraling at relativistic velocities along a strong co-aligned magnetic field. Here it is interesting to point out that the observed magnetic field, which according to the VLA mapping by Beck et al. (2005) is closely aligned with the bar just in the central regions, is turning its direction toward the nuclear engine.

According to the CO(2 – 1) SMA mapping by Sakamoto et al. (2007), there is in the outer torus also a “molecular cloud hot spot” co-located with the synchrotron jet source “F”, which has an intensity peak at a velocity that is inconsistent with the expected streaming motion in the torus. If the CO(2 – 1) hot spot at F were a “mirror image” of the one at D – moving along the circumnuclear torus – its line of sight (LOS) velocity, according to Table 2, is expected to be  $\approx 1613 + (1613 - 1560) = 1666$

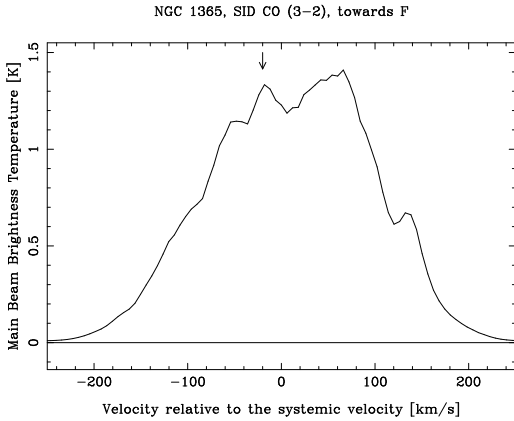
$\text{km s}^{-1}$ . However, its observed peak emission LOS velocity is  $1590 \text{ km s}^{-1}$ , that is,  $\approx 76 \text{ km s}^{-1}$  “too low” and “blue shifted” versus the systemic velocity by  $1613 - 1590 = 23 \text{ km s}^{-1}$ . This points at the existence of a molecular gas outflow from the nuclear engine, oriented along the direction of the nuclear synchrotron radiation jet. The peak emission is LOS blue-shifted by about  $25 \text{ km s}^{-1}$  with respect to the systemic velocity. This suggests the presence of a rather collimated molecular outflow, having a de-projected velocity of about  $70 \text{ km s}^{-1}$  in the same direction as the synchrotron jet, and which perhaps is driven by the same launching process (see Table 3). In fact, also Combes et al. (2019) propose the possibility of a nuclear outflow, observed in the ALMA CO(3 – 2) velocity field, similar to that found for NGC 613 (Audibert et al. 2019). We here compare the CO(2 – 1) profile observed at  $2''$  resolution in radio source F (Fig. 11 of Sakamoto et al. 2007), displaying a pronounced rather narrow peak at  $1590 \text{ km s}^{-1}$  on top of a broader range ( $1500 - 1750$

Table 3. Physical parameters of NGC 1365 compared with those of NGC 1377.

Object	Rotation Outflow P.A.[ $^{\circ}$ ]	or Axis Incl.[ $^{\circ}$ ]	Radius or Size [kpc/pc]	Rotation or Outflow Vel. [km s $^{-1}$ ]	Mass Dyn. <sup>a</sup> [ $\times 10^9 M_{\odot}$ ]	Gas <sup>b</sup>	Period or Age [Myr]	Remarks
<b>NGC 1365</b>								
Disk <sup>c</sup>	130	50	22	$\approx 270$	360	13	$\approx 500$	H I mass
Bar <sup>c,d</sup>		50	10	180	13 <sup>d</sup>		340	Stellar mass
Disk		50	10	310	220	9	200	H <sub>2</sub> mass
Disk			2	310	44	2.8	40	
Disk/torus <sup>b</sup>			1	230	12	2.4	27	“Star formation gas ring”, with solid body rotation
Outer torus	$\approx 130$	$\approx 50$	800	185	6		27	as visualized in Fig. A.1
Outer torus			500	115	1.5		27	
<i>Nuclear engine:</i>								
Inner torus <sup>d</sup>	$\approx 160$	$\approx 63$	26	$\approx 100$	0.06	0.007	1.6	Note torus axis tilt <sup>d</sup> , caused by $\approx 30^{\circ}$ precession angle
<b>Black Hole<sup>d</sup></b>								
<i>Nuclear outflows:</i>								
Radio Jet <sup>c,e</sup>	$\approx 135$	$\approx 20$	$\approx 400$	0.7c?				Table 2; Inclination caused by nuclear engine tilt
CO outflow <sup>f</sup>	$\approx 135$	$\approx 20$ ( $\approx 80$ )	$\approx 400$ ( $\approx 2200$ )	$\approx 70$ ( $\approx 23$ )			5.9 (90)	Sect. 4.3.1 & ref d); Inclination by nuclear engine tilt
O III bi-cone <sup>g</sup>	130	50	$\pm 2500$	$\pm 200$	–	0.001	$\approx 12$	Unlikely inclination alternative; See Sect. 4.3.2
H I outflow	$\approx 160$		2000	$\pm 200$			$\approx 10$	Hollow, wide angle ( $\pm 50^{\circ}$ ) ionized gas “fountain” Fig. 7; Desorption/dissociation from icy grains?
<b>NGC 1377</b>								
Nuclear disk <sup>h</sup>	15	$\approx 0$	29	75	0.04	0.017		
CO outflow <sup>h</sup>	15	$\approx 0$	200	140	–	0.01 – 0.05	1.4	Opening angle $\approx 60 - 70^{\circ}$
Map area <sup>i</sup>	15	$\approx 0$	–	–	–	0.16		Size: $4'' \times 4''$
Accretion disk <sup>j</sup>	15	$\approx 0$	$\approx 10$	110	0.03	0.018	$\approx 1$	Rotation period
Bipolar CO Jet <sup>j</sup>	15	$\pm(10 - 25)^k$	$\pm 150$	240 – 850 <sup>m</sup>	–	0.002 – 0.02 <sup>m</sup>	0.2 – 0.7	Precession Period: 0.3 – 1.1

<sup>(a)</sup>

This paper, Eq.(2). <sup>(b)</sup> This paper, Sect. 4.1. <sup>(c)</sup> Lindblad (1999). <sup>(d)</sup> Combes et al. (2019), who (in their Table 4) list an inner torus tilt, with an uncertainty of  $\pm 10^{\circ}$ . <sup>(e)</sup> Sandqvist et al. (1995). <sup>(f)</sup> This paper, Table 2 & Sect. 4.3.2. <sup>(g)</sup> Hjelm & Lindblad (1996); Lindblad (1999); Venturi et al. (2018). <sup>(h)</sup> Aalto et al. (2012). <sup>(i)</sup> Aalto et al. (2016). <sup>(j)</sup> in Ref. (j) estimated precession angle of CO jet and nuclear engine. <sup>(m)</sup> interval depending upon precession angle.



**Fig. 10.** SID CO(3 – 2) profile toward the continuum source “F”. The arrow indicates a weak and narrow feature, possibly indicative of the molecular outflow, discussed in Sect. 4.3.1

km s<sup>-1</sup>) pedestal, with our 5'' resolution CO(3 – 2) spectrum in the same direction. This is shown in Fig. 10, where the arrow indicates a narrow feature. The weakness of the presumptive molecular jet emission at  $\approx -25$  km s<sup>-1</sup>, observed at 5'' resolution may suggest that the extent of this emission is  $\leq 2''$ , equivalent circular size in the plane of the sky, that is, indicating a collimated, molecular gas outflow of size  $4'' \times < 1''$ .

The envisioned  $\approx 400$  pc size relativistic synchrotron jet and collimated molecular outflow are enshrouded by a kpc size fan-or, rather, cone-shaped ionized gas outflow, revealed by its visual O III emission (Hjelm & Lindblad 1996, discussed in considerable detail in the review paper by Lindblad 1999). More recently, this hollow wide-angle ( $\approx 100^\circ$ ) outflow of ionized gases has been studied in considerable detail by Lena et al. (2016) and Venturi et al. (2018). From their optical high spectral resolution mapping of the central 5 kpc ( $60'' \times 60''$ ) region of NGC 1365, at a spatial resolution of 70 pc ( $0.76''$ ), by means of VLT MUSE (multi-unit spectroscopic explorer), paired with Chandra X-ray data and elaborate analyses, Venturi et al. (2018) revealed the very inhomogeneous and anisotropic structure of the mass outflow rate and the velocity field of this bi-conical, wide angle,  $\pm 2.5$  kpc size, nuclear outflow of ionized gases, having velocities up to 200 km s<sup>-1</sup>. Their Fig. 7, displaying the estimated ionized gas mass outflow rate at 5'' (450 pc) resolution, demonstrates very pronounced radial as well as angular variations in the range ( $10^{-5} - 10^{-2}$ )  $M_\odot/\text{yr}$ . From a consideration of the kinetic energy rate and the momentum rate of the extended outflow of ionized gas and the mass outflow rate available from the AGN, obtained from their Chandra X-ray data, Venturi et al. argue that the extended ionized gas outflow must be momentum powered, that is, driven by the X-ray pressure (i.e., by X-ray photon collisions with the dust component of the gas). The authors also point out that the expected multiple supernova explosions (SNe) in the “star formation ring”, the outer torus in our nomenclature, may also contribute to the powering and temporal variation of the very extended ( $\pm 2.5$  kpc), wide angle ( $\pm 50^\circ$ ), bi-conical nuclear outflow. This is especially so since the observed outflow extent is as large as the diameter ( $\leq 2$  kpc) of the outer torus, while the diameter of the AGN accretion disk (the inner torus) is only  $\approx 50$  pc (see our Table 3). A main reason for the radial variations of the ionized gas may be found in the observed variable

nuclear X-ray emission causing (temporal) variations in the outflow launching radiation pressure. We return to the likely cause of the angular variations in Sect. 4.3.2. While SNe-induced multiple “chimney processes” presumably are in action in the outer torus (as modeled by e.g., Norman & Ikeuchi 1989; Melioli et al. 2009), the larger scale “nuclear fountain” scenario may be the main driver (as modeled by e.g., Wada 2012, 2015; Wada et al. 2016).

In Fig. 7(1) it may be seen that there is an  $\approx 20''$  H I absorption ridge emanating from the nucleus, in a south-southeast direction. This H I ridge can also be followed in the four individual maps shown in Fig. 8, implying that the ridge has a very wide velocity dispersion ( $\approx 400$  km s<sup>-1</sup>). This H I ridge coincides in position with the southern edge of the O III cone and may have arisen by the action of collisions of the outflow-driving X-ray photons with the dust grains. This interaction most likely would cause the water ice covering the cold dust grain surfaces to be desorbed and subsequently cause the water vapor to be dissociated into 2H + O. It is here interesting to note that, according to Fig. 7 of Venturi et al. (2018), the mass outflow rates of ionized gas are observed to be especially high along P.A.  $\approx 135^\circ$  and  $\approx 160^\circ$ , that is, in the direction of the synchrotron radiation and molecular gas jet as well as along the elusive H I absorption ridge just discussed. Here it may be interesting to note that the H I ridge may well be accompanied by a low level wide velocity CO(3 – 2) emission ridge at P.A.  $\approx 160^\circ$ , as hinted in Fig. 7(2).

The very wide velocity dispersion of the H I absorption ridge, mentioned above, with both negative and positive velocity components is perplexing, but not completely surprising. Hjelm & Lindblad (1996) found that the southeastern edge of their O III cone had also shown a “split” structure with both negative and positive velocity components in a velocity range similar to the H I ridge (see their observations with slits 6, 7, 10, and 11 in their Fig. 6). This was interpreted as contributions from both the outflow cone and the disk. A first approximation to the H I column density,  $N(\text{H I})$ , in the H I ridge can be obtained from  $N(\text{H I})/T_s = 1.823 \times 10^{18} \times \tau \times \Delta V$  (cm<sup>-2</sup>K<sup>-1</sup>), where  $T_s$  is the spin temperature, and the optical depth of the H I absorption is  $\tau = -\ln[1 + (I_{\text{H I}})/(I_c)]$ ,  $I_{\text{H I}}$  (a negative number) and  $I_c$  are the intensities of the H I absorption line and continuum, respectively, in mJy/beam (Sandqvist 1974). The beam for the H I observations is  $11''.6 \times 6''.3$ , and the continuum has been estimated from Fig. 6 of Sandqvist et al. (1995) and corrected to the H I resolution. A second approximation has been made using the continuum observations in Fig. 7 of Beck et al. (2002), also adjusted to the H I resolution. The results for two positions in the H I ridge are presented in Table 4.

Using the canonical H I spin temperature of 100 K, we may now estimate an H I column density for the H I ridge of a few  $\times 10^{21}$  cm<sup>-2</sup>. For the maximum H I integrated emission region in Fig. 7, located near the position of the H II hot spot L4, we determine an H I column density of  $6 \times 10^{22}$  cm<sup>-2</sup>, using the conversion factor given by Jörsäter & van Moorsel (1995) – a column density value similar to that found for the +50 km s<sup>-1</sup> cloud in the Sgr A complex in the center of our own galaxy (Sandqvist 1974).

In support of our own forthcoming scenario proposal in Sect. 4.3.2, we now will turn to the very interesting SMA and ALMA results presented by Aalto et al. (2012, 2016). Their CO(2 – 1) SMA observations at a resolution of  $\approx 0.6''$  of the lenticular spiral galaxy NGC 1377, at a distance of 21 Mpc where  $1'' \approx 102$  pc, – very similar to the parameters of NGC 1365 – revealed an extended molecular outflow and an orthogonal nuclear disk – outflow extent  $\approx 200$  pc, opening angle of  $60^\circ - 70^\circ$ , outflow

**Table 4.** H I column densities in the H I absorption ridge.

Source	Offsets ( $\Delta\alpha, \Delta\delta$ )	$I_{\text{H I}}$ [mJy/beam]	$\Delta V$ [km s <sup>-1</sup> ]	$I_1$ [mJy/beam]	$I_2$ [mJy/beam]	$\tau_1$	$\tau_2$	$N_1/T_s$ [cm <sup>-2</sup> K <sup>-1</sup> ]	$N_2/T_s$ [cm <sup>-2</sup> K <sup>-1</sup> ]
H I ridge top	(+2'', -9'')	-0.45	380	5.2	14.5	0.091	0.032	$6.3 \times 10^{19}$	$2.2 \times 10^{19}$
H I ridge bottom	(+7'', -15'')	-0.65	340	5.2	14.5	0.13	0.045	$8.3 \times 10^{19}$	$2.8 \times 10^{19}$

velocity  $\approx 140$  km s<sup>-1</sup> and mass  $\approx (1 - 5) \times 10^7 M_\odot$ ; dynamical versus molecular nuclear disk masses  $\approx 4 \times 10^7 M_\odot$  versus  $1.7 \times 10^7 M_\odot$ ).

From their analysis of the ALMA CO(3 - 2) observations at 0.2'' resolution, and maximum recoverable structure size of 5'', Aalto et al. (2016) discovered a very collimated molecular jet, counter-jet system of size  $\pm 150$  pc, displaying velocity reversals along the jets with a swing of  $\pm 150$  km s<sup>-1</sup>. This was interpreted and satisfactorily modeled as a precessing bi-polar jet system, having a precession angle  $\approx 10 - 25^\circ$  around a direction along the plane of the sky, precession period  $\approx 0.3 - 1.1$  Myr, outflow velocity  $\approx 240 - 850$  km s<sup>-1</sup>, and outflow mass  $\approx (0.2 - 2) \times 10^7 M_\odot$ . The outflow rate was estimated to be  $\approx 10 M_\odot/\text{yr}$  – a value they considered to be very uncertain. The molecular mass in the entire 4''  $\times$  4'' map was estimated to be  $16 \times 10^7 M_\odot$ . The rotational velocity of an accretion disk of size  $\approx 10$  pc was estimated to be  $\approx 110$  km/s, which implies a rotation period of  $\approx 1$  Myr. This in fact provides a lower limit to the jet precession period, which must be larger than the rotation period of its launching accretion disk. The more relevant physical parameters have been collected in our Table 3, for comparison with our scenario in NGC 1365.

Aalto et al. (2016) propose that their elusive, gaseous precessing jet, counter-jet system is likely to be powered by faint bipolar “radio jets”, that is, by relativistic plasma outflows suffering from energy losses by synchrotron radiation, as was described earlier, or alternatively by an accretion disk-wind similar to those found toward proto-stars. The latter case also includes discussions of analogous MHD models of precessing bi-polar outflows, powered by the accretion onto a proto-star – a jet precession which has been observed, for example, in L1551 IRS5 and IRAS 16293-2422 (Fridlund & Liseau 1994; Kristensen et al. 2013). Aalto et al. (2016) also carefully discuss the various scenarios which may cause the observed molecular jet precession, with at-the-point references. Their favored alternatives are: i) misalignment between the spin orientation of the SMBH and the rotation axis of the surrounding accretion disk, or ii) an accretion inflow of gas having misaligned angular momentum.

#### 4.3.2. Tilted massive inner torus of cold gas – a precessing nuclear engine?

Scrutinizing the various observed and calculated physical parameters collected in Table 3, we note two problematic issues where nature, however, has provided elegant and efficient solutions. The first one is the “angular momentum problem” at the formation of a compact object – in our case a central black hole, while a very similar problem appears in proto-stellar formation – as illustrated by the rotation time column. While the rotation time of the galaxy disk falls in the range 500 – 40 Myr, the bar-induced outer torus, having a radius of 400 – 1000 pc and a cold gas mass of  $\approx 2 \times 10^9 M_\odot$ , is rotating almost as a solid body with a revolution time of 27 Myr. This outer torus is encircling a much smaller inner torus, accretion disk of radius 26 pc and estimated

cold gas mass of  $\approx 7 \times 10^6 M_\odot$  and a rotation time of  $\approx 1.6$  Myr – in its turn surrounding a rapidly spinning SMBH having a mass of  $\approx 4 \times 10^6 M_\odot$  (Combes et al. 2019; Risaliti et al. 2013). To overcome the “angular momentum problem” nature has found a solution here to the energy balance problem in terms of MHD launching of a relativistic plasma outflow, which is observable because of its synchrotron radiation loss, and a co-existing collimated molecular gas (CO) outflow. It has also launched the directly observable X-ray emission from the nuclear engine, which in addition is causing the observed very extended wide angle ionized gas outflow by the action of its radiation pressure.

With these facts in mind, we arrive at the second problem in case of NGC 1365. While the symmetry axis of the hollow wide angle ionized gas outflow appears to coincide with the rotation axis of the galaxy disk and the outer torus (P.A. = 130°; Incl. = 50°), the rotation axis of the inner torus, black hole nuclear engine (P.A. = 160°  $\pm$  10°; Incl. = 63°  $\pm$  10°) according to the model fit of CO(3 - 2) ALMA data by Combes et al. (2019), deviates by  $\approx 30^\circ \pm 10^\circ$  from the common direction. The direction of the synchrotron radiation jet, collimated molecular gas outflow is observationally known only in terms of its P.A.  $\approx 135^\circ$ . However, to allow the previously outlined powering scenario of the synchrotron radiation jet, collimated CO outflow, the rotation axis of the nuclear engine must have agreed with the outflow direction at an earlier time. If we consider these facts, the only realistic alternative seems to be that the inner torus is precessing, at an assumed precession angle of  $\approx 30^\circ$ , around the common rotation axis of the galaxy disk and the outer torus. The precession period must be larger than the inner torus rotation period of 1.6 Myr and presumably be lower than the rotation period of the outer torus, 27 Myr. The inclination of the synchrotron radiation, CO jet in this scenario must be  $\approx 50^\circ \pm 30^\circ$ , that is, Incl. = 20°, or 80°, where the former case results in an outflow size of 400 pc, a reasonable outflow velocity of 70 km s<sup>-1</sup> and an outflow age of  $\approx 6$  Myr. The other alternative must be considered unlikely because of the resulting very large size and age (see Table 3). Since the rotation axis of the accretion disk must have precessed (in the same direction as the rotation of the outer and inner tori) by about 75% of its period from its launching of the synchrotron jet, molecular outflow to its current position, we may now estimate the precession period of the nuclear engine to be about 8 Myr, which is well below the rotation period of the outer torus, 27 Myr.

This scenario solves not only the launching of the synchrotron, CO jet but may also help to explain the angular mass loss rate inhomogeneity of the wide angle ionized gas outflow observed by Venturi et al. (2018). In addition the proposed inner torus precession scenario provides a natural solution of the problem that the bi-conical outflow is covering a very wide sector (P.A.  $\approx 80^\circ - 180^\circ$ ) even at a radius of 2.5 kpc, which corresponds to a launch time of 25 – 50 Myr at an estimated outflow velocity of 100 – 50 km s<sup>-1</sup> and is hollow, that is, with little or no outflow near the symmetry axis (cf. Hjelm and Lindblad



1996). This is not well accommodated by state of the art theoretical modeling of nuclear outflow fountains (e.g., Wada 2015). A precession angle of  $\approx 25 - 30^\circ$  and a bi-conical outflow sector of  $\pm 25^\circ$  should here be able to do the required job of supporting the observed ionized outflow, created during several precession periods.

At first sight a precession angle as large as  $20^\circ - 40^\circ$  may seem unrealistic. However, the ALMA observations of NGC 1377 by Aalto et al. (2016), paired with their careful analysis, lead to a required accretion disk precession angle of  $10^\circ - 25^\circ$ . The physical reason for the suggested inner torus precession in NGC 1365 could be “an accretion inflow of gas having misaligned angular momentum”, which is the previously mentioned second alternative for NGC 1377 of Aalto et al. (2016), since the outer torus of NGC 1365 is asymmetric and very inhomogeneous in its mass distribution. As shown in Table 3, the accretion tori of NGC 1365 and NGC 1377 have similar sizes, rotation times and cold gas masses.

#### 4.4. Discussion of the H<sub>2</sub>O emissions in NGC 1365 versus those in other galaxies

The outer circumnuclear torus region and the nuclear region contain all the ingredients necessary to locally raise the gas-phase water abundance to levels which are several orders of magnitude higher than the quiescent, cold cloud value of  $8 \times 10^{-10}$  versus H<sub>2</sub>, assuming an ortho-to-para ratio of 3. Here most H<sub>2</sub>O is likely to reside as water ice on cold grain surfaces (e.g., van der Tak et al. 2010).

We have in Table 5 collected the results from our spatially unresolved but spectrally resolved *Odin* observations of the 557 GHz ground state o-H<sub>2</sub>O line. There are also the results from spectrally unresolved, but spatially partly resolved, *Herschel* SPIRE multi-transition H<sub>2</sub>O and CO mapping observations, for comparison with: i) *Odin* ground state o-H<sub>2</sub>O and o-H<sub>2</sub><sup>18</sup>O results for our Galactic center region, Sgr A (Karlsson et al. 2013), ii) *Herschel* HIFI, SPIRE, and PACS results for the merger NGC 6240 (with galaxy-wide shocks; Meijerink et al. 2013, Liu et al. 2017), and iii) the results from a detailed radiative transfer and excitation analysis of a sample of other galaxies extensively observed by *Herschel* HIFI, SPIRE, and PACS (Liu et al. 2017; Gonzalez-Alfonso et al. 2010, 2012).

In addition to the comparisons between galaxies provided in Table 5, we have in an Appendix B included a Table B.1 comparing our estimated H<sub>2</sub>O abundances in NGC 1365 with more detailed Sgr A results, as well as with observed H<sub>2</sub>O abundances in a number of well-known types of Galactic molecular cloud regions, where also detailed chemical models are established. For the interested reader a short summary of current chemical models of water formation and destruction is also included in this Appendix.

##### 4.4.1. Comments to Table 5

###### NGC 1365:

**A)** *Odin* observes very weak ground state o-H<sub>2</sub>O emission from dense molecular cloud complexes located in the circumnuclear torus region in the velocity range 1400 – 1650 km s<sup>-1</sup> – an emission which in a velocity range around 1500 km s<sup>-1</sup> suffers from absorption caused by the low excitation, foreground cloud envelopes of the cloud core emission plus the thermal dust continuum background. Taking into account the source size, approximately 15'', and location of maximum emission apparent

from the *Herschel* SPIRE mapping, we find that the integrated H<sub>2</sub>O intensities observed by *Odin* and *Herschel* agree very well, and that the velocity range of the *Odin* emission is as expected for emission from the NE torus region.

The existence of water absorption by lower excitation cloud envelopes most likely can be ascribed to the PDR chemistry, including grain surface reactions, in action in such regions. The water emission from the massive complexes of cloud cores, co-located with super starburst clusters and H II regions residing in the NE torus region of NGC 1365 (cf. Elmegreen et al. 2009), is bound to originate from a combination of PDR chemistry, including grain surface reactions, quiescent warm molecular cloud ion-molecule chemistry, and also hot cores. There is possibly influence by an increased ionization level caused by cosmic ray focusing by the aligned magnetic field, as mapped by Beck et al. (2005), and locally also by X-ray emission from the star forming superclusters. Outflow and shock chemistry may also contribute to the ground state o-H<sub>2</sub>O emission (see next Comment).

**B)** The CO and H<sub>2</sub>O emissions from the higher energy states appear to be best explained by shock excitation. While the CO-SLED can be nicely matched by a two-component model using 40 – 60 K for the lower energy lines and requiring a low velocity ( $\approx 10$  km s<sup>-1</sup>) shock at a pre-shock density of  $10^4$  cm<sup>-3</sup> to reach the observed intensities of the higher energy lines. The H<sub>2</sub>O-SLED seems to require a high velocity ( $\approx 40$  km s<sup>-1</sup>) shock at a pre-shock density of about  $10^4$  cm<sup>-3</sup>, using the shock model by Flower & Pineau de Fôrets (2010) (cf. Comment G for the merger NGC 6240). There is probably a requirement also for some radiative Far IR (FIR) excitation, which was used to model the *Herschel* SPIRE observations of H<sub>2</sub>O in the ULIRGs Mrk 231, NGC 4418 and Arp 220 by Gonzalez-Alfonso et al. 2010, 2012, as discussed in Sect. 4.2.2.

If FIR excitation were dominating, the required H<sub>2</sub>O abundance would be a factor of 10 – 100 times lower than the fast shock (40 km s<sup>-1</sup>) model abundance of  $10^{-4}$  versus H<sub>2</sub> (Gonzalez-Alfonso et al. 2010, 2012, 2014; Flower & Pineau de Forêts 2010). This is an abundance level achievable by low velocity shock chemistry including shock release of icy grain mantles. However, no PACS observations of the FIR pumping water vapor absorption lines are available in case of NGC 1365.

###### Sgr A:

**C)** This is absorption in the low excitation  $-30$  km s<sup>-1</sup> foreground spiral arm. The PDR chemistry, including grain surface reactions, is the likely explanation for the observed water abundance. However, the possible *Herschel* HIFI detection of the 487 GHz O<sub>2</sub> line in this spiral arm tells us that a ( $\approx 20$  km s<sup>-1</sup>) Galactic spiral arm density wave shock also may be in action (cf. Sandqvist et al. 2015).

**D)** The emissions from the warm and dense  $+20$  km s<sup>-1</sup>,  $+50$  km s<sup>-1</sup>, and CND (circumnuclear disk, torus) cloud cores are resulting from PDR chemistry, including grain surface reactions, quiescent cloud ion-molecule chemistry, and possibly hot cores.

**E)** These H<sub>2</sub>O line wings, not suffering from self-absorption, associated with the  $+20$  km s<sup>-1</sup>,  $+50$  km s<sup>-1</sup>, and CND clouds must be caused by shock chemistry as well as shock desorption, sputtering from icy grain mantles.

###### NGC 6240:

**F)** This is emission from warm cloud complexes in the merger interface region.

**G)** This is most likely emission from “galaxy-wide shocks”. Meijerink et al. (2013) found that the CO-SLED, observed by *Herschel* SPIRE, is best modeled by a ( $\approx 10$  km s<sup>-1</sup>) shock

**Table 5.** Comparison of NGC 1365 and other galaxies.

Object	Region	Density ( $\text{cm}^{-3}$ )	Gas / Dust Temperature (K)	H <sub>2</sub> O abundance vs H <sub>2</sub> ( $\times 10^{-8}$ )	Comments
NGC 1365 (Barred spiral)	absorption <sup>a</sup>	$10^2 - 10^4$	$\approx 20^c$	5 – 8	A
	emission <sup>a,b</sup>	$10^4 - 10^6$	40 – 60/55 <sup>c</sup>	6 – 600 <sup>i,k</sup>	A
	shocks <sup>b</sup>	$10^4 - 10^{5d}$	350/22 – 32 <sup>c</sup>	200 <sup>n</sup> – 10,000 <sup>l</sup>	B
Sgr A <sup>e</sup>	absorption	$10^2 - 10^{3i}$	100 – 30 <sup>i</sup> /15 <sup>m</sup>	3	C
	emission	$10^4 - 10^{5f}$	80 <sup>f</sup> /20 – 30 <sup>m</sup>	2 – 7	D
	line wings	$3 \times (10^4 - 10^5)$	80 – 160/20 – 30 <sup>m</sup>	80 – 570	E
NGC 6240 (Merger <sup>g,h</sup> )	warm emission	$10^6$	60 – 70/60 – 70	10	F
	shocks	$5 \times (10^4 - 10^6)^d$	120 – 400/20 – 30	10	G
Galaxy sample <sup>h</sup>	absorption	$10^3 - 10^5$	20 – 200/20 – 30	0.1 – 10	H, J
	cold emission	$10^3 - 10^5$	20 – 30/20 – 30	0.1 – 1	H
	warm emission	$10^5 - 10^6$	40 – 70/40 – 70	1 – 10	H
	hot emission	$10^5 - 10^6$	100 – 200/100 – 200	100 – 1000	K

<sup>(a)</sup> This paper – *Odin* observations of ground state o-H<sub>2</sub>O (see text). <sup>(b)</sup> This paper – *Herschel* SPIRE mapping observations plus modeling (see text). <sup>(c)</sup> Dust temperatures from Alonso-Herrero et al. (2012) and Tabatabaei et al. (2013). <sup>(d)</sup> Pre-shock density; The post-shock density becomes an order of magnitude higher. <sup>(e)</sup> from *Odin* observations of ground state o-H<sub>2</sub>O and o-H<sub>2</sub><sup>18</sup>O, assuming an ortho-to-para ratio of 3 (Karlsson et al. 2013). <sup>(f)</sup> from Walmsley et al. (1986). <sup>(g)</sup> from *Herschel* SPIRE observations (Meijerink et al. 2013). <sup>(h)</sup> from *Herschel* HIFI, SPIRE and PACS observations (Liu et al. 2017). <sup>(i)</sup> from the Sandqvist et al. (2015) *Herschel* HIFI 487 GHz search for O<sub>2</sub>. <sup>(j)</sup> the abundance scales  $\approx$  inversely with cloud density <sup>(k)</sup> lower abundances may be accommodated by PDR models, while the high ones indicate shocks (see Comments). <sup>(l)</sup> fast shock model abundance (Flower & Pineau de Forêts 2010) in an effective accumulated 10'' size area (see Comments). <sup>(m)</sup> from Sandqvist et al. (2008). <sup>(n)</sup> from slow shock chemistry, in case FIR pumping dominates (Gonzalez-Alfonso et al. (2010, 2012, 2014).

excitation and a pre-shock density of  $5 \times 10^4 \text{ cm}^{-3}$ , leading to a post-shock density of  $4 \times 10^5 \text{ cm}^{-3}$ . They also point out that the 2  $\mu\text{m}$  H<sub>2</sub> emission, observed at the merger central region, requires a shock in the velocity range 47 – 16  $\text{km s}^{-1}$  for a pre-shock density of  $5 \times 10^5 - 10^7 \text{ cm}^{-3}$ . See also the H<sub>2</sub>O SLED analysis by Liu et al. (2017) and the discussion of NGC 6240 in their Appendix.

*Other galaxies observed by HIFI, SPIRE and PACS aboard Herschel Space Observatory:*

**H)** These results were based upon multi-transition CO and H<sub>2</sub>O SLEDs as well as dust SED observations by *Herschel* HIFI, SPIRE, and PACS, paired with extensive radiative transfer and excitation modeling, including collisional as well as radiative excitation, see Liu et al. (2017).

**J)** Similarly to what is visualized by the *Odin* 557 GHz ground state o-H<sub>2</sub>O spectrum of NGC 1365, emission plus absorption is often seen in the observed *Herschel* HIFI ground state o-H<sub>2</sub>O spectra, and are even more frequent in the *Herschel* HIFI 1113 GHz ground state p-H<sub>2</sub>O spectra (van der Tak et al. 2016; Liu et al. 2017). It may be interesting to note that the 1113 GHz line is not clearly visible and not claimed to be detected in our NGC 1365 SPIRE data.

**K)** Only for the most infrared luminous galaxies Mrk 231, NGC 4418, and Arp 220, these compact hot gas, dust components were required to fit the observational data. Here the high temperature, possibly caused by shocks, leads to efficient release of H<sub>2</sub>O from the icy grain surfaces into the gas phase, hence explaining the high gas phase abundance of water. In addition, X-ray emission from the AGN, or from a nuclear star burst, may provide a contribution by XDR chemistry. FIR excitation ap-

pears to be very important in these galaxies (Liu et al. 2017; Gonzalez-Alfonso et al. 2010, 2012).

#### 4.4.2. Some conclusions concerning the H<sub>2</sub>O emission and absorption regions in galaxies

The ortho and para ground state rotational transitions of H<sub>2</sub>O at 557 and 1113 GHz often exhibit sharp absorption features caused by lower excitation foreground gas – where the water vapor content of  $\approx 10^{-9} - 10^{-8}$  versus H<sub>2</sub> is resulting from PDR chemistry – intersecting broad velocity emission from the denser molecular cloud ensemble – caused by a mixture of PDR and “hot core” chemistries and possibly also is influenced by shock sputtering and shock chemistry. These processes all rely upon the release of icy grain mantles and result in average H<sub>2</sub>O abundances of  $\approx 10^{-8} - 10^{-7}$ .

The rotationally excited state H<sub>2</sub>O emissions, observed by *Herschel* HIFI and SPIRE, appear to be best explained by a combination of FIR and shock excitation, where FIR excitation is likely to be dominating in the ULIRGs. Shock chemistry and shock release of icy grain mantles are the likely processes causing the estimated very high H<sub>2</sub>O abundances of  $\approx 10^{-6} - 10^{-4}$ , with possible influences from “hot core chemistry” in regions of very extensive star formation.

The FIR H<sub>2</sub>O lines at shorter wavelengths, observed by *Herschel* PACS, all have very high critical densities for collisional excitation and therefore are bound to be “FIR pumped”. The very high H<sub>2</sub>O abundances of  $10^{-6} - 10^{-5}$ , estimated from these observations, are likely to result from efficient release of icy grain mantles, caused by varying combinations of “hot cores” near massive young stars, shock sputtering, and XDR chemistry

caused by intense X-ray emission, as well as shock chemistry – all depending upon the environmental conditions in the galaxy in question.

#### 4.5. Methylidyne radical, CH, and its ion CH<sup>+</sup> – probable signatures of shocks and intense UV-illumination in the NGC 1365 circumnuclear torus region

We here enter a discussion of the presence of CH as well as CH<sup>+</sup> in the circumnuclear torus region, as is revealed by the SPIRE spectrum (Fig. 3 and Table 1) and by our CH and CH<sup>+</sup> maps, shown in Fig. 4. While an emission line at 835.1 GHz nicely matches the  $J = 1 - 0$  rotational transition of CH<sup>+</sup> in its <sup>1</sup>Σ electronic ground state, CH in its <sup>2</sup>Π electronic ground state appears in terms of two emission doublets, at 532.7/536.8 GHz and 1470.7/1477.4 GHz, classified as the ( $1_{3/2}^+ \rightarrow 1_{1/2}^- / 1_{3/2}^- \rightarrow 1_{1/2}^+$ ) and ( $2_{3/2}^- \rightarrow 1_{3/2}^+ / 2_{3/2}^+ \rightarrow 1_{3/2}^-$ ) transitions, respectively (with quantum states denoted  $N_J^{parity}$ ). More details are given in Appendix C, and an energy level diagram can be found in Rangwala et al. (2014). These CH transitions are caused by a step-wise internal energy decay of the CH molecular population from the Λ-doubled second lowest ( $N = 2, J = 3/2$ ) rotationally excited state (at  $E_u \approx 96.5$  K) to the Λ-doubled lowest ( $N = 1, J = 3/2$ ) rotationally excited state (at  $E_u \approx 25.7$  K), and subsequently to the Λ-doubled <sup>2</sup>Π ( $N = 1, J = 1/2$ ) CH ground state. Here the rather obvious, and simplest, contributing excitation mechanism would be “direct radiative pumping” causing population transport from the  $N = 1, J = 1/2$  ground state Λ-doublet state to the  $N = 2, J = 3/2$  rotationally excited Λ-doublet state by means of CH absorptions of the thermal dust emission at 2006.8/2010.8 GHz ( $\approx 149 \mu\text{m}$ ), that is, close to the thermal emission maximum of dust at a temperature of  $\approx 20$  K, as is observed in NGC 1365 (Figs. 1 and 2). However, no proof in terms of such observed 149  $\mu\text{m}$  CH absorptions is available in NGC 1365, but appears to have been observed in the ( $L_{\text{FIR}} \approx 10^{12} L_{\odot}$ ) ULIRG, Arp 220, by *Herschel* PACS, as reported in the SPIRE and HIFI based CH analysis by Rangwala et al. (2014).

Arp 220 is a late-stage merger with two closely located counter-rotating disks and also was included in the multi-line H<sub>2</sub>O analysis by Liu et al. (2017), where it together with Mrk 231 required a hot and dense gas component to fit the observed H<sub>2</sub>O-SLED (cf. our Table 5 and its comments). Stepwise collisional CH excitation may also be contributing processes, which then would require the high gas densities and temperatures resulting from the shocks which are observed to be in action in the many hot spots of the outer circumnuclear torus of NGC 1365 (Galliano et al. 2012; Fazeli et al. 2019) and here were crucial for the H<sub>2</sub>O and CO excitation (see Sect. 4.2.2). Extensive shocks and star formation-induced outflows also are likely to be present in Arp 220, as well as in the IR bright ( $L_{\text{FIR}} \approx 2 \times 10^{11} L_{\odot}$ ) Seyfert 2 galaxy NGC 1068 (Spinoglio et al. 2012; Liu et al. 2017), which will be our forthcoming CH, CH<sup>+</sup> comparison galaxy.

The CH assignment of the striking 532.7/536.8 GHz line doublet requires some carefulness, since unfortunately the laboratory frequencies of the HCN(6 – 5) and HCO<sup>+</sup>(6 – 5) lines at 531.7 and 535.1 GHz are almost overlapping, considering the poor SPIRE spectral resolution and the broad galaxy spectral lines. However, there are no visible signs of the HCN(7 – 6) and HCO<sup>+</sup>(7 – 6) lines in our NGC 1365 SPIRE spectrum, which limits their contribution to our CH doublet to be at most about 20 %. This is consistent with the comparatively small contributions from HCN and HCO<sup>+</sup> found by Rangwala et al. (2014) in

their complementary *Herschel* HIFI observations of a number of galaxies, including Arp 220.

From the *Herschel* SPIRE line intensities listed in Table 1, we estimate the upper state column densities of the 533/537 GHz and 1471/1477 GHz CH doublets to be  $23 \times 10^{12} \text{ cm}^{-2}$  and  $15 \times 10^{12} \text{ cm}^{-2}$ , for an assumed, accumulated source size of 14″. We can then determine an excitation (population distribution) temperature for these states to be  $T_{\text{ex}} \approx 75$  K. This allows us to calculate the total column density in the four lowest rotational states to be  $\approx 8 \times 10^{13} \text{ cm}^{-2}$ , under the assumption of a common excitation temperature. The estimated excitation temperature is in fact a lower limit since the 533/537 GHz doublet may contain some HCN/HCO<sup>+</sup> emission and is at least as high as the kinetic temperature of the quiescent molecular clouds, which suggests influences of FIR pumping and/or efficient collisional excitation in the observed shock regions.

In the same way, we estimate the upper ( $J = 1$ ) state column density of CH<sup>+</sup> to be  $1.6 \times 10^{12} \text{ cm}^{-2}$ , for an assumed source size of 14″ (Fig. 4). The minimum total CH<sup>+</sup> column density is estimated to be  $\approx 3.5 \times 10^{12} \text{ cm}^{-2}$  for excitation temperatures in the range 40 to 100 K (cf. Falgarone et al. 2010b). However, in view of the intense UV-illumination from newly formed stars, the CH<sup>+</sup> column density may well be an order of magnitude larger, approaching that of CH. The reason is formation by the reaction between C<sup>+</sup> and vibrot-excited H<sub>2</sub>, which also causes a large enhancement of the rotationally excited CH<sup>+</sup> states, as has been observed in the Orion Bar (Nagy et al. 2013, 2017; see also Appendix C). In the case of NGC 1365 we have to rely on the observed existence of multiple vibrot H<sub>2</sub> lines in the hot spots of the outer torus region, and the existence of strong UV radiation in these regions of intense star formation (Galliano et al. 2012; Fazeli et al. 2019). For these reasons we may estimate the CH/CH<sup>+</sup> abundance ratio to be  $\leq 23$ .

From the simultaneously observed SPIRE maps (Fig. 4), it appears that the H<sub>2</sub>O and CH<sup>+</sup> emissions peak in the NE torus region while the CO and CH emissions are more evenly distributed across the circumnuclear torus. The higher energy CO-SLED is nicely modeled by a low velocity (10 km s<sup>-1</sup>) shock, which also may satisfactorily explain the required CH excitation as well as its high abundance in denser gas (see Appendix C). The higher velocity (40 km s<sup>-1</sup>) shock, possibly required to model the H<sub>2</sub>O-SLED in the NE torus region, paired with the intense UV radiation from the observed massive young stellar superclusters (Galliano et al. 2012) may explain the previously discussed possible overabundance of CH<sup>+</sup> (Gerin et al. 2016; Godard et al. 2019; see also Appendix C).

With these uncertainties in mind, we now proceed to estimate the CH and CH<sup>+</sup> abundances. Here a comparison H<sub>2</sub> column density is available from our multi-transition SPIRE-CO modeling in Sect. 4.2.2. Correcting the model value  $N(\text{CO}) \approx 4 \times 10^{15} \text{ cm}^{-2}$  for the beam filling of a 14″ source size in a 40″ antenna beam, and assuming a CO/H<sub>2</sub> abundance ratio of 10<sup>-4</sup>, we arrive at an average of  $N(\text{H}_2) \approx 4 \times 10^{20} \text{ cm}^{-2}$  for the shocked gas regions of the outer torus. The CH and CH<sup>+</sup> abundances then become  $X(\text{CH}) \approx 2 \times 10^{-7}$  and  $X(\text{CH}^+) \approx 10^{-8}$ . In the unlikely case that the emissions were originating in the quiescent molecular clouds, these abundances would be lower by a factor of about 30.

Only in NGC 1068, out of the four prototypical AGN or star burst dominated galaxies (NGC 1068, Arp 220, M82 and NGC 253) selected for *Herschel* CH observations by Rangwala et al. (2014), did both the CH and the CH<sup>+</sup> lines appear in emission, similar to our case of NGC 1365. In the other galaxies, CH<sup>+</sup> was observed in absorption, presumably from lower excita-

tion foreground gas, while CH was observed in emission (from higher density regions). Our IR luminous comparison galaxy, NGC 1068 ( $L_{\text{FIR}} \approx 2 \times 10^{11} L_{\odot}$ ), is exhibiting a number of similarities with NGC 1365 ( $L_{\text{FIR}} \approx 5 \times 10^{10} L_{\odot}$ ), that is, a circumnuclear torus – a prominent “star forming molecular cloud ring” of radius 1 – 1.5 kpc versus  $\approx 0.8$  kpc in NGC 1365 – and a smaller circumnuclear disk – CND of radius 100 – 150 pc versus  $\approx 26$  pc in NGC 1365 – as discussed in more detail by Spinoglio et al. (2012) and Liu et al. (2017).

The CH abundance estimated in NGC 1068 by Rangwala et al. (2014), from the 533/537 GHz doublet alone, is  $\approx 10^{-8}$  versus  $\text{H}_2$ . The CH/CH<sup>+</sup> abundance ratio is found to be  $\approx 23$ , just as in NGC 1365, however in both cases somewhat uncertain values because of lacking observations of the molecular excitation. The NGC 1068 abundances were nicely accommodated by XDR physics, chemistry in the CND, driven by the X-ray emission from the AGN. A similar inner torus generated XDR emission of CH and CH<sup>+</sup> is likely to exist also in NGC 1365. However, here the dominant parts of the CH and CH<sup>+</sup> emissions are located to the UV-illuminated shock regions of the outer torus, as is strongly indicated by our observed emission maxima at the NE torus FIR and molecular gas mass peak. In the absence of *Herschel* Space Observatory, improved knowledge of the CH and CH<sup>+</sup> molecular population distributions in NGC 1365, as well as in NGC 1068, could here be achieved by spectrally resolved *Sofia* limited mapping observations of the CH doublet at 2 THz and the CH<sup>+</sup> ( $J = 2 - 1$ ) transition at 1669 GHz.

In this context the results from *Herschel* PACS observations of multiple OH<sup>+</sup>, H<sub>2</sub>O<sup>+</sup>, and H<sub>3</sub>O<sup>+</sup> absorption lines in the ULIRGs, NGC 4418 and Arp 220, by Gonzalez-Alfonso et al. (2013) are useful to contemplate, since the importance of an observed molecular population distribution is emphasized. It turned out that in the single case of Arp 220 the pure inversion, metastable state lines of H<sub>3</sub>O<sup>+</sup> revealed a very high population distribution temperature of  $\approx 500$  K, indicating hot gas or “formation pumping”. There, excess energy from the H<sub>3</sub>O<sup>+</sup> formation process leaves the resulting molecule in a high rotational temperature molecular state distribution). The population distributions of OH<sup>+</sup> and H<sub>2</sub>O<sup>+</sup> did not show such an anomaly. These results are very important for the understanding of the molecular formation processes in question. However, no OH<sup>+</sup>, H<sub>2</sub>O<sup>+</sup> or H<sub>3</sub>O<sup>+</sup> signals can be identified in our NGC 1365 SPIRE spectrum (Fig. 3 and Table 1).

In the light of our current discussion of CH and CH<sup>+</sup> observations and their modeling interpretations, and including the results from the very recent modeling of UV irradiated molecular shocks by Godard et al. (2019), inspired by the ALMA discovery of CH<sup>+</sup>(1 – 0) emission and absorption lines from a number of lensed star burst galaxies at a redshift of  $\approx 2.5$  (Falgarone et al. 2017) – we are inclined to believe that the CH and CH<sup>+</sup> emission lines observed from the circumnuclear torus region of NGC 1365 are signposts of shock action in this region, presumably penetrated by intense UV light and molecular outflows caused by the observed extensive star formation.

## 5. Summary and conclusions

We have used the *Odin* satellite to observe the central region of the barred spiral galaxy NGC 1365 in the 557 GHz H<sub>2</sub>O line. After a total of 81 hours of ON-source integration time, we have obtained a marginal detection of this water vapor line at a velocity resolution of 5 km s<sup>-1</sup>. We have combined these observations with *Herschel* PACS and SPIRE observations of two positions in the galaxy’s nucleus, obtained from the *Herschel* Science

Archive, and produced simultaneously observed SPIRE images of the distribution of o-H<sub>2</sub>O, p-H<sub>2</sub>O, CO, CH, CH<sup>+</sup>, and N II.

The water vapor emission is predominantly located in the shocked 15'' (1.3 kpc) region of the northeastern (NE) component of the molecular torus surrounding the nucleus. Here, several compact radio sources, hot-spot H II regions, as well as co-located very massive molecular cloud complexes, and young stellar superclusters have been observed – all of which triggered by the rapid bar-driven inflow into the circumnuclear torus, causing cloud-cloud collisions and shocks. The two ground state H<sub>2</sub>O emission components, detected in the *Odin* spectrum, have approximate velocities of  $-150$  and  $-40$  km s<sup>-1</sup> with respect to the systemic velocity of the galaxy, while an intersecting absorption appears at a velocity of  $-100$  km s<sup>-1</sup>, which agrees with kinematic studies of the bar-driven circumnuclear torus gas flow in the vicinity of the NE component. For the absorbing gas region, we find an H<sub>2</sub>O fractional abundance of  $\geq 5 \times 10^{-8}$ , which is well accommodated by PDR chemistry. In the presumably denser emission regions, the H<sub>2</sub>O abundance appears to increase but may still be understood in terms of PDR chemistry taking place in this region of strong UV radiation from the young super star clusters. However, part of the ground state H<sub>2</sub>O emission may also be caused by shock excitation and chemistry, as will be discussed next.

Model studies of the multi-transition SPIRE CO and H<sub>2</sub>O observations toward the NE component reveal the presence of a slow-velocity C-type shock with a shock speed of 10 to 40 km s<sup>-1</sup> and an H<sub>2</sub> pre-shock density of  $10^4$  cm<sup>-3</sup>, where the lower velocities are sufficient to model the observed CO spectral line energy distribution (SLED). The observed H<sub>2</sub>O SLED requires the higher shock velocities, which are also sufficient to drive the vibrational excitation of H<sub>2</sub>. In addition, FIR pumping may be required to satisfactorily explain the H<sub>2</sub>O SLED. A model abundance versus H<sub>2</sub> of  $10^{-4}$  was reached for CO as well as for H<sub>2</sub>O. If the H<sub>2</sub>O excitation were dominated by FIR pumping, the required H<sub>2</sub>O abundance is lower by a factor of 10 – 100 and is most likely caused by slow velocity shock chemistry (as discussed in Sect. 4.2.2 and Appendix B).

While the H<sub>2</sub>O and CH<sup>+</sup> emissions seem to be concentrated near the NE torus component, the CO and CH emissions appear to be more evenly distributed between the NE and the SW torus component, as revealed by the SPIRE images. These relative distributions may reflect the fact that the eastern bar-driven gas inflow into the NE torus region is much more massive than the corresponding gas inflow from the western bar into the SW torus region. In the case of CH we estimate an abundance of  $2 \times 10^{-7}$ . The estimated CH<sup>+</sup> abundance of  $\approx 10^{-8}$  in the NE torus region is likely to be a lower limit because of (here unconfirmed) formation via the abundant vibrationally and rotationally excited H<sub>2</sub> in this shock and UV irradiated region. Such a CH<sup>+</sup> abundance enhancement has indeed been observed in the Orion Bar (See Appendix C).

We have made a statistical image deconvolution (SID) of our single dish SEST observations of the CO(3 – 2) emission in the nuclear region of NGC 1365, yielding an angular resolution of 5'', complementing recent ALMA observations. These SID observations yield dynamical masses of  $1.2 \times 10^{10} M_{\odot}$  and  $4.4 \times 10^{10} M_{\odot}$  inside radii of 1 and 2 kpc, respectively, where the gas mass amounts to  $\approx 20\%$  in the inner region and  $\approx 6\%$  in the region inside 2 kpc.

We discuss a co-located collimated CO jet, a relativistic radio jet and a wide-angle inhomogeneous ionized O III gas cone outflow from the nuclear engine. Our VLA H I absorption analysis reveals an H I ridge extending from the nucleus in a south-

southeast direction, coinciding with the southern edge of the O III cone. With an H I column density of a few  $\times 10^{21}$  cm<sup>-2</sup>, this ridge may have been created by the action of outflow-driving X-ray photons colliding with dust grains, causing water ice from the dust grains to be desorbed and dissociated into 2H + O. A precessing nuclear engine appears to be required to accommodate the various outflow components, and is also consistent with the ALMA observations by Combes et al. (2019) of a tilted massive inner gas torus or accretion disk.

**Acknowledgements.** First of all we wish to thank Per Olof Lindblad for many valuable discussions and his numerous comments on the manuscript of this paper. We also wish to thank the anonymous referee for the careful reading of the manuscript and the many constructive comments, which much improved our paper. For valuable contributions in the late-stage preparation of the *Odin* satellite observing program and its successful operation, we wish to thank H.-G. Floren at Stockholm Observatory, M. Battelino and B. Jakobsson at OHB Sweden, G. Persson at Onsala Space Observatory and S.-O. Silverlind at the Swedish Space Corporation in Esrange.

## References

- Aalto, S., Hüttemeister, S., Scoville, N. Z., & Thaddeus, P. 1999, *ApJ*, 522, 165  
Aalto, S., Müller, S., Sakamoto, K., et al. 2012, *A&A*, 546, A68  
Aalto, S., Costagliola, F., Müller, S., et al. 2016, *A&A*, 590, A73  
Alloin, D., Edmunds, M. G., Lindblad, P. O., & Pagel, B. E. J. 1981, *A&A*, 101, 377  
Alonso-Herrero, A., Sanchez-Portal, M., Ramos Almeida, C., et al. 2012, *MN*, 425, 311  
Arce, H. G., Shepherd, D., Gueth, F., et al. 2007, *Molecular Outflows in Low- and High-Mass Star-forming Regions*, in *Protostars and Planets V*, ed. B. Reipurth, D. Jewitt, & K. Keil, (University of Arizona Press, Tucson), 245  
Armijos-Abendano, J., Martin-Pintado, J., Requena-Torres, M. A., et al. 2019, *arXiv:1902.05098*  
Audibert, A., Combes, F., García-Burillo, S., et al. 2019, *A&A*, 632, A33  
Beck, R., Shoutenkov, V., Ehle, M., et al. 2002, *A&A*, 391, 83  
Beck, R., Fletcher, A., Shukurov, A., et al. 2005, *A&A*, 444, 739  
Bergin, E. A., Melnick, G. J., & Neufeld, D. A. 1998, *ApJ*, 499, 777  
Black, J. H., & Dalgarno, A. 1973, *ApL*, 15, 79  
Blandford, R. D., & Begelman, M. C. 1999, *MNRAS* 303, L1  
Bohlin, R. C., Savage, B. D., & Drake, J. F. 1978, *ApJ*, 224, 132  
Combes, F., García-Burillo, S., Audibert, A., et al. 2019, *A&A*, 623, A79  
Curran, S. J., Polatidis, A. G., Aalto, S., & Booth, R. S. 2001, *A&A*, 368, 824  
Elmegreen, B. G., Galliano, E., & Alloin, D. 2009, *ApJ*, 703, 1297  
Falgarone, E., Godard, B., Cernicharo, J., et al. 2010a, *A&A*, 521, L15  
Falgarone, E., Ossenkopf, V., Gerin, M., et al. 2010b, *A&A*, 518, L118  
Falgarone, E., Zwaan, M. A., Godard, B., et al. 2017, *Nature*, 548, 430  
Farquhar, P. R. A., Millar, T. J., & Herbst, E. 1994, *MNRAS*, 269, 641  
Fazeli, N., Busch, G., Valencia-S., M., et al. 2019, *A&A*, 622, 128  
Flower, D. R. & Pineau des Forêts, G. 2003, *MNRAS*, 343, 390  
Flower, D. R. & Pineau des Forêts, G. 2010, *MNRAS*, 406, 1745  
Flower, D. R., Le Bourlot, J., Pineau des Forêts, G., & Cabrit, S. 2003, *MNRAS*, 341, 70  
Fridlund, C.V.M.; & Liseau, R. 1994, *A&A*, 292, 631  
Frisk, U., Hagström M., Ala-Laurinaho, J., et al. 2003, *A&A*, 402, L27  
Galliano, E., Alloin, D., Pantin, E., et al. 2005, *A&A*, 438, 803  
Galliano, E., Alloin, D., Pantin, E., et al. 2008, *A&A*, 492, 3  
Galliano, E., Kissler-Patig, M., Alloin, D., & Telles, E. 2012, *A&A*, 545, A10  
García-Burillo S., Combes, F., Usero, A., et al. 2014, *A&A*, 567, A125  
Gerin, M., de Luca, M., Goicoechea, J. R., et al. 2010, *A&A*, 521, L16  
Gerin, M., Neufeld, D. A., & Goicoechea, J. R. 2016, *ARA&A*, 54, 181  
Godard, B., & Cernicharo, J. 2013, *A&A*, 550, A8  
Godard, B., Pineau des Forêts, G., Lesaffre, P., et al. 2019, *A&A*, 622, A100  
Goldsmith, P. F., & Langer, W. D. 1978, *ApJ*, 222, 881  
González-Alfonso, E., Fischer, J., Isaak, K., et al. 2010, *A&A*, 518L, 43  
González-Alfonso, E., Fischer, J., Graciá-Carpio, J., et al. 2012, *A&A*, 541, A4  
González-Alfonso, E., Fischer, J., Bruderer, S., et al. 2013, *A&A*, 550, A25  
González-Alfonso, E., Fischer, J., Aalto, S., & Falstad, N. 2014, *A&A*, 567, A91  
Herbst, E., & Leung, C. M. 1986a, *MNRAS*, 222, 689  
Herbst, E., & Leung, C. M. 1986b, *ApJ*, 310, 378  
Hjalmarson, Å.; & Friberg, P. 1988, *ASIC*, 241, 65  
Hjalmarson, Å., Sume, A., Elldér, J., et al. 1977, *ApJS*, 35, 263  
Hjalmarson, Å., Frisk, U., Olberg, M., et al. 2003, *A&A*, 402, L39  
Hjalmarson, Å., Bergman, P., Biver, N., et al. 2005, *AdSpR*, 36, 1031  
Hjelm, M., & Lindblad, P.O. 1996, *A&A*, 305, 727  
Hollenbach, D., Kaufman, M. J., Bergin, E. A., & Melnick, G. J. 2009, *ApJ*, 690, 1497  
Hollenbach, D., Kaufman, M. J., Neufeld, D., Wolfire, M., & Goicoechea, J. R. 2012, *ApJ*, 754, 105  
Irvine, W. M., Goldsmith, P. F., & Hjalmarson, Å. 1987, *ASSL*, 134, 561  
Jörsäter, S., & van Moorsel, G. A. 1995, *AJ*, 110, 2037  
Karlsson, R., Sandqvist, Aa., Hjalmarson, A., et al. 2013, *A&A*, 554, A141  
Kristen, H., Jörsäter, S., Lindblad, P. O., & Boksenberg, A. 1997, *A&A*, 328, 483  
Kristensen, L. E., Ravkilde, T. L., Field, D., Lemaire, J. L., & Pineau des Forêts, G. 2007, *A&A* 469, 561  
Kristensen, L. E., Klaassen, P.D., Mottram, J.C., Schmalzl, M., & Hogerheijde, M. R. 2013, *A&A*, 549, L6  
Königl, A., & Pudritz, R. E. 2000, *Disk Winds and the Accretion-Outflow Connection*, in *Protostars and Planets IV*, ed. V. Mannings, A. P. Boss, & S. S. Russell, (University of Arizona Press, Tucson), 759  
Langer, W. D., Goldsmith, P. F., & Pineda, J. L. 2016, *A&A*, 590, 43  
Lena, D., Robinson, A., Storchi-Bergmann, T., et al. 2016, *MNRAS*, 459, 4485  
Lin, C. C., & Shu, F. H. 1964, *ApJ*, 140, 646  
Lindblad, P. O. 1960, *Stockholms observatoriums annaler*, 21, bd 3  
Lindblad, P. A. B., Lindblad, P. O., & Athanassoula, E. 1996, *A&A*, 313, 65  
Lindblad, P. O., Hjelm, M., Högbom, J., et al. 1996, *A&AS*, 120, 403  
Lindblad, P. O. 1999, *A&AR*, 9, 221  
Liu, L., Weiss, A., Perez-Beaupuits, J. P., et al. 2017, *ApJ*, 846:5  
Madore, B. F., Freedman, W. L., Silbermann, N., et al. 1998, *Nat*, 395:3, 47  
Meijerink, R., & Spaans, M. 2005, *A&A*, 436, 397  
Meijerink, R., Spaans, M., & Israel, F. P. 2007, *A&A*, 461, 73  
Meijerink, R., Kristensen, L. E., Weiss, A., et al. 2013, *ApJ*, 762L, 16  
Melioli, C., Brighenti, F., D'Ercole, A., & de Gouveia Dal Pino, E. M. 2009, *MNRAS*, 399, 1089  
Melnick, G. J., Tolls, V., Neufeld, D. A., et al. 2008, *ApJ*, 683, 876  
Melnick, G. J., Tolls, V., Neufeld, D. A., et al. 2010, *A&A*, 521, L27  
Mitchell, G. F. 1984, *ApJS*, 54, 81  
Morris, P.W.; Gupta, H.; Nagy, Z.; et al. 2016, *ApJ*, 829, 25  
Nagy, Z.; van der Tak, F.F.S.; Ossenkopf, V.; et al. 2013, *A&A*, 550, A96  
Nagy, Z.; Choi, Y.; Ossenkopf-Okada, V.; et al. 2017, *A&A*, 559, A22  
Nayakshin, S. 2014, *MNRAS*, 441, 1380  
Neill, J. L., Wang, S., Bergin, E. A., et al. 2013, *ApJ*, 770, 142  
Neufeld, D. A., Lepp, S., & Melnick, G. J. 1995, *ApJS*, 100, 132  
Nilsson, A., Hjalmarson, Å., Bergman, P., & Millar, T. J. 2000, *A&A*, 358, 257  
Norman, C. A., & Ikeuchi, S. 1990, *ApJ*, 343, 372  
Olofsson, A. O. H., Olofsson, G., Hjalmarson, Å., et al. 2003, *A&A*, 402, L470  
Persson, C. M., Olofsson, A. O. H., Koning, N., et al. 2007, *A&A*, 476, 807  
Persson, C. M., Olberg, M., Hjalmarson, Å., et al. 2009, *A&A*, 494, 637  
Persson, C. M., Maoli, R., Encenaz, P., et al. 2010, *A&A*, 515, A72  
Pfenninger, D., & Norman, C. 1990, *ApJ*, 363, 391  
Pinol Ferrer, N., Lindblad, P. O., & Fathi, K. 2012, *MNRAS*, 421, 1089  
Rangwala, N., Maloney, P. R., Glenn, J., et al. 2014, *ApJ*, 788, 147  
Risaliti, G., Harrison, F. A., Madsen, K. K., et al. 2013, *Nature*, 494, 449  
Rodgers, S. D., & Charnley, S. B. 2001, *ApJ*, 546, 324  
Roberts, W. W. Jr., & Stewart, G. R. 1987, *ApJ*, 314, 10  
Rydbeck, G. 2008, *ApJ*, 675, 1304  
Rydbeck, G., Hjalmarson, Å., & Rydbeck, O.E.H. 1985, *A&A*, 144, 282  
Rydbeck, O. E. H., Elldér, J., & Irwine, W. M. 1973, *Nature* 246, 466  
Rydbeck, O. E. H., Kollberg, E., Hjalmarson, Å., et al. 1976, *ApJS*, 31, 333  
Sakamoto, K., Ho, P. T. P., Mao, R.-Q., Matsushita, S., & Peck, A. B. 2007, *ApJ*, 654, 782  
Sandqvist, Aa. 1974, *A&A*, 33, 413  
Sandqvist, Aa. 1999, *A&A*, 343, 367  
Sandqvist, Aa., Jörsäter, S., & Lindblad, P. O. 1995, *A&A*, 295, 585  
Sandqvist, Aa., Larsson, B., Hjalmarson, Å., et al. 2008, *A&A*, 482, 849  
Sandqvist, Aa., Larsson, B., Hjalmarson, Å., et al. 2015, *A&A*, 584, A118  
Schinnerer, E., Weiß, A., Aalto, S., & Scoville, N. Z. 2010, *ApJ*, 719, 1588  
Scoville, N. Z., Sanders, D. B., & Clemens, D. P. 1986, *ApJ*, 310, L77  
Shu, F. H., Milone V., & Roberts, W.W.Jr. 1973, *ApJ*, 183, 819  
Snell, R. L., Howe, J. E., Ashby, M. L., et al. 2000, *ApJ*, 539, L101  
Spinoglio, L., Pereira-Santaella, M., Busquet, G., et al. 2012, *ApJ*, 758, 108  
Stacey, G. J., Lugten, J. B., & Genzel, R. 1987, *ApJ*, 313, 859  
Sundelius, B., Thomasson, M., Valtonen, M.J., & Byrd, G.G. 1987, *A&A*, 174, 67  
Swinyard, B. M., Ade, P., Baluteau, J.-P., et al. 2010, *A&A*, 518, L4  
Tabatabaei, F. S., Weiss, A., Combes, F., et al. 2013, *A&A*, 555, A128  
Takahashi, H., Hollenbach, D.J., & Silk, J. 1985, *ApJ*, 292, 192  
Toomre, A. 1964, *ApJ*, 139, 1217  
Turner, B. E. 1988, *ApJ* 329, 425  
Turner, B. E., & Zuckerman, B. 1974, *ApJ*, 187L, 59  
van der Tak, F. F. S., Black, J. H., & Schöier, F.L. 2007, *A&A*, 468, 627  
van der Tak, F. F. S., Marseille, M. G., Herpin, F., et al. 2010, *A&A*, 518, L107  
van der Tak, F. F. S., Weiss, A., Liu, L., & Güsten, R. 2016, *A&A*, 593, A43  
van Dishoeck, E. F., & Blake, G. A. 1998, *ARA&A*, 36, 31  
van Dishoeck, E. F., Herbst, E., & Neufeld, D. A. 2013, *ChRv*, 113, 9043  
Venturi, G. M., Nardini, E., Marconi, A., et al. 2018, *A&A*, 619, A74  
Wada, K. 2012, *ApJ*, 758, 66  
Wada, K. 2015, *ApJ*, 812, 82  
Wada, K., Schartmann, M., & Meijerink, R. 2016, *ApJ*, 828, L19  
Walmsley, C. M., Güsten, R., Angerhofer, P., et al. 1986, *A&A*, 155, 129  
Whiteoak, J. B., Gardner, F. F., & Höglund, B. 1980, *MNRAS*, 190, 17  
Wiesemeyer, H., Güsten, R., Menten, K. M., et al. 2018, *A&A*, 612, 37  
Wilson, C. D., Mason, A., Gregersen, E., et al. 2003, *A&A*, 402, L59  
Wirstrom, E. S., Bergman, P., Olofsson, A. O. H., et al. 2006, *A&A*, 453, 979  
Yang, C., Gao, Y., Omont, O., et al. 2013, *ApJ*, 771, L24  
Zhao, Y., Lu, N., Xu, C. K., et al. 2016, *ApJ*, 819, 69  
Ziurys, L. M., & Turner, B. E. 1985, *ApJ*, 292L, 25

## Appendix A: VLA H<sub>1</sub> and SEST SID CO (3 – 2) position-velocity maps

Position-Velocity (P-V) maps of our VLA H<sub>1</sub> and SEST SID CO (3 – 2) observations, oriented parallel to the major axis of NGC 1365, are presented in Fig. A.1.

## Appendix B: On interstellar water chemistry

### Appendix B.1: Water abundances in NGC 1365 vs Galactic prototype regions

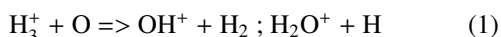
In Table B.1 we compare our current NGC 1365 H<sub>2</sub>O abundance estimates with recent *Odin* results for the Galactic Center Sgr A region (Karlsson et al. 2013), and with *Odin* and *Herschel* HIFI results for the local Orion molecular cloud (to demonstrate observationally determined H<sub>2</sub>O abundances caused by the PDR, warm cloud core, Hot Core, bipolar outflow and shock chemistries which are likely to be present also in the central regions of NGC 1365). For comparison we also list *Herschel* and *Odin*/SWAS results for the cold dense cores of the Galactic molecular clouds DR 21 and W 3 and for the S 140 PDR interface region.

### Appendix B.2: Water chemistry in cold and warm regions

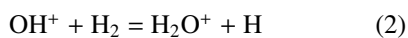
To make our discussion of the interstellar H<sub>2</sub>O chemistry going on in the central regions of NGC 1365 more to the point, we here provide a very simplified summary of the main formation and destruction routes, for cases where the theoretical models are well established (for details we refer to the extensive review paper by van Dishoeck et al. 2013) and where a sample of relevant observed H<sub>2</sub>O abundances have been listed in Table B.1.

#### Appendix B.2.1: Low temperature gas-phase water chemistry

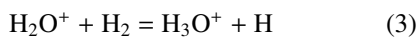
The oxygen chemistry is initiated by cosmic-ray (CR) ionization of H<sub>2</sub> which rapidly leads to the formation of the trihydrogen ion (H<sub>3</sub><sup>+</sup>). Next step is



followed by



and, subsequently,



followed by dissociative recombination,



but also ( $\approx 83\%$ )  $\text{OH} + \text{H}_2 ; \text{OH} + 2\text{H} ; \text{O} + \text{H}_2 + \text{H}$ .

At low temperatures the main loss of gaseous H<sub>2</sub>O is via accretion (adsorption, “sticking”) onto cold dust grain surfaces (where water ice has been observed to be a main constituent). Only at grain temperatures of 100 K, or higher, the H<sub>2</sub>O molecules are efficiently desorbed (evaporated) from the icy grain surfaces. While the just (crudely) described ion-molecule reaction scheme, for a standard Galactic CR flux, is capable of

producing a gas-phase H<sub>2</sub>O abundance  $X(\text{H}_2\text{O}) \approx 10^{-6} - 10^{-7}$  versus H<sub>2</sub>, the “freeze out” on cold grain surfaces may reduce this abundance by several orders of magnitude, as is illustrated in Table B.1 by the observed values of  $(1 - 2) \times 10^{-9}$  in the DR 21 and W 3 molecular cloud cores.

The expected gas-phase H<sub>2</sub>O abundance is closely related to the H<sub>3</sub><sup>+</sup> production. An increase of the CR flux leads to a faster chemistry, and also results in higher H<sub>3</sub><sup>+</sup> and H<sub>2</sub>O abundances (cf. Farquhar et al. 1994; Nilsson et al. 2000, on-line Figs. 16 and 21). In NGC 1365 we have already envisioned a probable CR focusing by the observed magnetic field aligned along the bar. Alternatively, X-ray ionization of H<sub>2</sub>, rapidly leading to enhanced H<sub>3</sub><sup>+</sup> abundance, also would do the same job. X-ray emission has indeed been observed in NGC 1365, especially in the nuclear region (from the central AGN, black hole region; see Lindblad 1999). Theory for XDR (X-ray Dominated Region) physics, chemistry has been developed by Meijerink & Spaans (2005) and has been applied to galaxy nuclei by Meijerink et al. (2007). Also an increased UV flux from one or more newly formed massive stars, influencing the surface layers of their mother molecular clouds and a developing H II region also is bound to produce an enhanced H<sub>2</sub>O abundance (theory by e.g. Hollenbach et al. 2009, 2012, who also study the influences of increased CR ionization). In Table B.1 we have listed observed H<sub>2</sub>O abundances of  $(5 - 10) \times 10^{-8}$  in the Orion PDR (Photon Dominated Region) interface layer between the molecular cloud and the M 42 H II region, and in the S 140 PDR. The water abundances of  $(2 - 3) \times 10^{-8}$ , observationally estimated for the DR 21 foreground cloud and the Sgr A  $-30 \text{ km s}^{-1}$  arm, both seen in absorption, also are likely results of PDR chemistry, but now in lower density regions of low visual extinction where the general Galactic background UV radiation can penetrate.

#### Appendix B.2.2: Ice chemistry

In parallel with the low temperature gas-phase chemistry, there are also ongoing grain surface reactions. In addition to the formation of H<sub>2</sub>, which requires a third body for its efficient formation, there are also a number of reactions (collisions) between atoms and molecules sticking on the grain surfaces, and jumping between the potential wells on the surface, hence forming ices containing H<sub>2</sub>O, CH<sub>3</sub>OH, NH<sub>3</sub>, CO, CO<sub>2</sub>, and CH<sub>4</sub>. To contribute to the gas-phase chemistry, these surface-sticking species need to be desorbed (evaporated, i.e., converted from solid state to gas-phase constituents). This desorption will require a grain temperature increase, which may be caused by absorption of the strong UV light from nearby newly formed stars, which is the case in PDR chemistry (Hollenbach et al. 2009) as well as in Hot Core chemistry (Rodgers & Charnley 2001). According to Table B.1 the observed H<sub>2</sub>O abundances are as high as  $10^{-5}$  and  $3 \times 10^{-6}$  in the high density Orion Hot Core (where  $T_{\text{kin}} \approx 200 \text{ K}$ ) and Compact Ridge (where  $T_{\text{kin}} \approx 115 \text{ K}$ ) regions, respectively.

#### Appendix B.2.3: High temperature water chemistry

Detachment of ice layers of grain-sticking molecules may also be caused by shocks, as may be the case in low velocity bi-polar outflows from young stars, supernova shocks and Galactic density wave shocks (cf. Flower & Pineau des Forêts 2003; Melnick et al. 2008). In Table B.1 we list observed gas-phase H<sub>2</sub>O abundances of a few  $\times 10^{-6}$  in the Orion and DR 21 low velocity outflows, and similar values for the red wing emissions from the Sgr A molecular cloud cores.

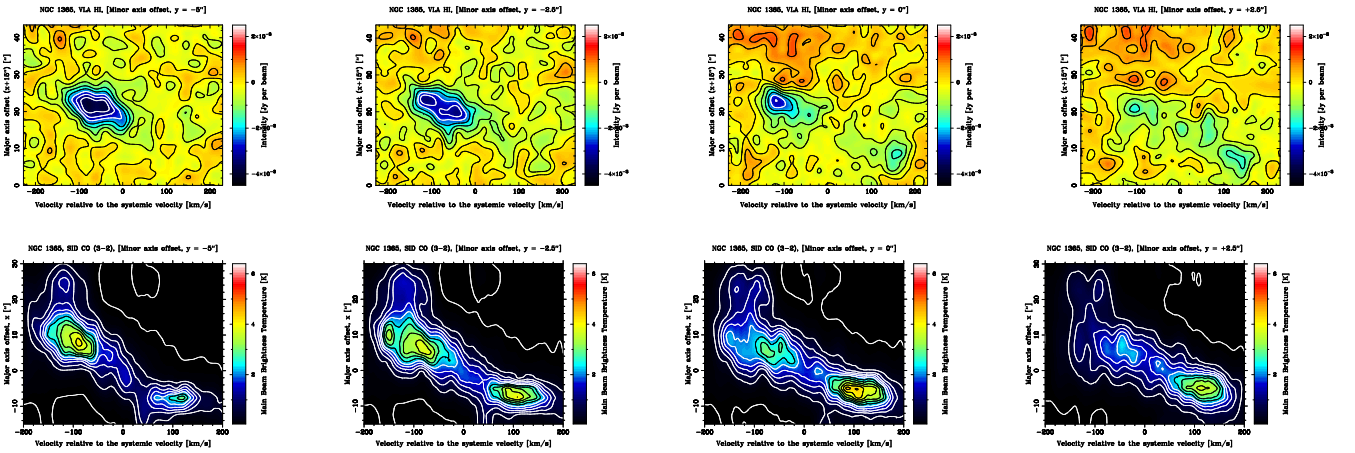
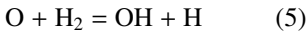
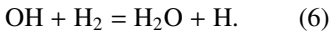


**Fig. A.1.** *[Top]*: VLA H I P-V maps oriented parallel to the major axis of NGC 1365 for different minor axis offsets ( $y = -5'', -2.5'', 0'', +2.5''$ ). The major axis offsets should be subtracted by  $15''$  to obtain the  $x$ -offsets from the optical nucleus, with positive values in the NE direction. *[Bottom]*: The SEST SID CO(3–2) P-V maps oriented parallel to the major axis of NGC 1365 for the same minor axis offsets as in the H I maps, with offsets ( $x, y$ ) being from the optical nucleus. The velocity offsets are with respect to  $1613 \text{ km s}^{-1}$ .

In addition to the evaporation of ices we also have to consider some key high temperature gas phase reactions, that is,



and subsequently



Shock heating and compression in this way may result in very high post shock gas-phase H<sub>2</sub>O abundances (cf. e.g., Bergin et al. 1998; Flower et al. 2003; Kristensen et al. 2007; Flower & Pineau de Forêts 2010), as illustrated in Table B.1 by an observationally determined  $X(\text{H}_2\text{O})$  versus shocked H<sub>2</sub> approaching  $3 \times 10^{-4}$  in the Orion high velocity outflow, where (almost) all elemental oxygen has been “locked-up” in gas-phase water. Here we should again remember that outflow driven shock excitation of H<sub>2</sub> has been observed by Galliano et al. (2012) in some of the circumnuclear torus hot spots of NGC 1365 (i.e., massive stellar clusters with their associated massive star forming gas clouds).

## Appendix C: Summary of the molecular physics and the interstellar chemistry of CH and CH<sup>+</sup>

An energy level diagram for CH is provided by Rangwala et al. (2014) and more detailed ones may be found in Rydbeck et al. (1976) and Turner (1988). The rotational levels of the light weight CH molecule appear in the submm/FIR range and show a doublet spectral line pattern caused by the splitting of the individual rotational state energies into  $\Lambda$ -doublets, resulting from the relative orientations of the orbital momentum axis of the unpaired  $\pi$  electron and the molecular rotation axis (being parallel or orthogonal, denoted as + or – parity). Magnetic hyperfine interaction further splits the  $\Lambda$ -doublet state energies, which was crucial for the identification of the interstellar radio transitions of CH, but causes overlapping lines and even difficult blends of emission and absorption at submm and FIR wavelengths. The observed doublet pattern of the rotational lines is the result of the quantum mechanical selection rule that a state parity change is required for an electric dipole transition to take place.

CH, CH<sup>+</sup>, and CN were the first interstellar molecules to be identified (in 1937–1941), via their absorption lines of the visual light from background stars (see the review by Gerin et al. 2016). The interstellar detection of the radio signals at  $\approx 3.3$  GHz from the three hyperfine transitions within the  $\Lambda$ -doubled  $^2\Pi(N = 1, J = 1/2)$  CH ground state was a matter of searches across a wide frequency range, since the frequencies were only very crudely known from molecular quantum mechanics applied to optical spectroscopy (Rydbeck et al. 1973; Turner & Zuckerman 1974). Subsequently the three CH hyperfine transitions were extensively observed and analyzed, and it was shown that these lines were weak masers (amplifying any background emission) in molecular cloud cores, cold dark clouds as well as in lower density spiral arm clouds (Rydbeck et al. 1976; Hjalmarson et al. 1977). The CH abundance versus H<sub>2</sub> was observed to decrease (from  $\approx 3 \times 10^{-8}$  to  $\approx 6 \times 10^{-10}$ ) with increasing cloud density, which may well be expected in regions where this reactive radical is consumed in the formation of more complex molecules, and also is consistent with more recent interstellar chemistry modeling (e.g., Herbst & Leung 1986 a,b). The lower satellite line of CH at 3264 MHz displayed an interesting anomaly in that its intensity rapidly increased with increasing FIR continuum emission, which was explained as “FIR pumping” and resulted from the parity structure of the  $\Lambda$ -doubled rotational states (Rydbeck et al. 1976). Subsequently CH detections in external galaxies could also be done, using the very sensitive maser receiver from Onsala Space Observatory installed on the Australian Parkes 64-m radio telescope (Whiteoak et al. 1980).

The first astronomical observation of CH in the far-infrared was performed by Stacey et al. (1987). Using NASA’s Kuiper Airborne Observatory they were able to detect the  $N = 1, J = 1/2$  ground state  $\Lambda$ -doublet to the  $N = 2, J = 3/2$  rotationally excited  $\Lambda$ -doublet state transitions of CH as an absorption line doublet at  $\approx 149 \mu\text{m}$  (2006.8/2010.8 GHz) against the FIR thermal dust emission of Sgr B2. These transitions are “always” expected to be observed in absorption since their critical densities for collisional excitation are  $> 10^{10} \text{ cm}^{-3}$ . Stacey et al. estimate the CH abundance versus H<sub>2</sub> to be  $\approx 10^{-9}$  for the Sgr B2 (denser) molecular cloud and  $\approx 10^{-7}$  for the (lower density) absorbing clouds in the 3 kpc arm and the expanding molecular ring. They also conclude that the enhanced 3264 MHz CH emission from the Sgr B2 molecular cloud must be primarily a FIR excitation

**Table B.1.** Comparison between observed H<sub>2</sub>O abundances in NGC 1365, our Galactic Center region (Sgr A) and some nearer Galactic sources.

Source (distance)	Region (kinetic temperature)	Abundance vs H <sub>2</sub> [ $\times 10^{-8}$ ]	
		<i>Odin</i> <sup>*</sup>	<i>Herschel</i>
NGC 1365 <sup>a</sup> (18.6 Mpc)	absorption ( $\approx 20$ K)	5 – 8	
	warm emission (40 – 60 K)	6 – 600 <sup>s</sup>	
	shocks (350 K)		200 <sup>u</sup> – 10,000 <sup>t</sup>
Sgr A <sup>d</sup> (8.7 kpc)	+50 km s <sup>-1</sup> Cloud (60 K)	5	
	Red wing of +50 km s <sup>-1</sup> Cloud <sup>e</sup>	130	
	CND (150 K) <sup>f</sup>	9	
	Red wing of CND <sup>e</sup>	760	100 – 1300 <sup>b</sup>
	+20 km s <sup>-1</sup> Cloud (60 K)	3	4 <sup>c</sup>
	Red wing of +20 km s <sup>-1</sup> Cloud <sup>e</sup>	110	
Orion KL <sup>m</sup> (450 pc)	-30 km s <sup>-1</sup> arm <sup>g</sup>	4	
	PDR interface region (70 K)	9 <sup>h,i</sup>	
	2' south core (75 K)	11 <sup>h,i</sup>	
	Compact Ridge (115 K)	280 <sup>j</sup>	260 <sup>k</sup>
	Hot Core (200 K)	1200 <sup>j</sup>	1000 <sup>l,k</sup>
	Low velocity outflow	290 <sup>j</sup>	480 <sup>k</sup>
	High velocity outflow (vs all H <sub>2</sub> )	2200 <sup>j</sup>	7000 <sup>l</sup>
DR 21 (1.7 kpc)	High velocity outflow (vs shocked H <sub>2</sub> )	10000 <sup>h</sup> 28000 <sup>j</sup>	
	Cool dense core (23 K)		0.1 <sup>n,o</sup>
	Foreground cloud (10 K)		2 <sup>n,o</sup>
W3 IRS 5 (2.3 kpc)	Low velocity outflow		280 <sup>n,o</sup>
	Cool dense core (40 K)	0.2 <sup>p</sup>	
S 140	Clumpy PDR interface with dark cloud (55 K)	5/0.1 <sup>q,r</sup>	
	Low velocity outflow	40 <sup>q</sup>	

(<sup>\*</sup>) based upon ortho-H<sub>2</sub>O, H<sub>2</sub><sup>18</sup>O and H<sub>2</sub><sup>17</sup>O (1<sub>10</sub> – 1<sub>01</sub>) observations; (<sup>a</sup>) this paper; (<sup>b</sup>) from *Herschel* mapping of the CND/Sgr A\* by Armijos-Abendano et al. (2019); (<sup>c</sup>) from *Herschel* mapping of the +20 km s<sup>-1</sup> Cloud by Armijos-Abendano et al. (2019); (<sup>d</sup>) from Karlsson et al. (2013), assuming an ortho-to-para ratio of 3; (<sup>e</sup>) outflow/shock; (<sup>f</sup>) Circumnuclear Disk (torus) surrounding the Sgr A\* black hole; (<sup>g</sup>) foreground spiral arm; (<sup>h</sup>) Olofsson et al. (2003); (<sup>i</sup>) Wirström et al. (2006); (<sup>j</sup>) *Odin* spectral scan, Persson et al. (2007); (<sup>k</sup>) *Herschel*/HIFI spectral scan, Neill et al. (2013); (<sup>l</sup>) Melnick et al. (2010); (<sup>m</sup>) mapped in detail by *Odin*, Hjalmarsen et al. (2005); (<sup>n</sup>) based upon para-H<sub>2</sub>O (1<sub>11</sub> – 0<sub>00</sub>) observations, van der Tak et al. (2010); (<sup>o</sup>) assuming an ortho-to-para ratio of 3; (<sup>p</sup>) from *Odin* mapping by Wilson et al. (2003) in close agreement with SWAS results by Snell et al. (2000); (<sup>q</sup>) clump/interclump values; (<sup>r</sup>) from *Odin* mapping by Persson et al. (2009). (<sup>s</sup>) the lower abundance estimates appear at higher densities and can be accommodated by PDR models, while the high abundances (at a density of 10<sup>4</sup> cm<sup>-3</sup>) would indicate that the existing shocks also contribute to the observed ground state H<sub>2</sub>O emission. (<sup>t</sup>) shock model abundance (Flower & Pineau des Forêts 2010) in an effective (accumulated) 10'' size area of the circumnuclear torus (see Sect. 4.4). (<sup>u</sup>) caused by slow velocity shock chemistry in the case of (here unconfirmed) dominant FIR excitation (Gonzalez-Alfonso et al. 2010, 2012, 2014).

effect. Recently much more detailed, higher spectral and spatial resolution, 2 THz CH absorption doublet studies toward a number of Galactic molecular clouds have been performed from SOFIA (the Stratospheric Observatory for Infrared Astronomy; Wiesemeyer et al. 2018).

The lowest rotationally excited CH ( $N = 1; J = 3/2$ ) state, only 25.7 K above the ground state, was detected by means of the very large 1000 foot (300 m) Arecibo and Green Bank 300 foot (91 m) telescopes in a number of molecular cloud cores, in terms of four hyperfine transitions within the  $\Lambda$ -doublet at  $\approx 700$  MHz, all seen in absorption (Ziurys & Turner 1985; Turner 1988). An interesting conclusion was that the CH abundance versus H<sub>2</sub> was

as high as  $2 \times 10^{-8}$  in regions of density  $2 \times 10^4$  cm<sup>-3</sup> – an abundance which was too high to be consistent with chemical models for dense quiescent clouds, but instead pointed at the action of shock chemistry. In fact, molecular outflows (causing shocks) have been observed in the regions considered. The results from the (early) modeling of low velocity shocks (5 – 20 km s<sup>-1</sup>) in dense (10<sup>4</sup> cm<sup>-3</sup>) gas clouds by Mitchell (1984) is a useful guideline here – and may be so also in our case of NGC 1365.

The detection of the CH 533/537 GHz transition doublet in the directions of several massive star-formation regions relied on *Herschel* HIFI observations, and revealed intriguing blends of absorptions from lower density (diffuse) spiral arm foreground



clouds and emission from the molecular cloud cores (Gerin et al. 2010). Thanks to the hyperfine splitting, nowadays known from laboratory spectroscopy, paired with molecular quantum mechanics the emission/absorption line pattern could be deconvolved. The CH abundance vs H<sub>2</sub> in the foreground clouds was determined to be  $\approx 3.5 \times 10^{-8}$  in clouds having densities in the range 100–1000 cm<sup>-3</sup> – an abundance consistent with the results from decades of optical CH absorption line observations, and precisely modeled by PDR chemistry (originating from Black & Dalgarno 1973; see Gerin et al. 2010 and Gerin et al. 2016 for a discussion and references). From their SOFIA observations and a careful analysis of the CH absorption line doublet at  $\approx 149 \mu\text{m}$  (from the ground state, just as the 533/537 GHz transitions) Wiesemeyer et al. (2018) confirm this conclusion, that is, that CH may be used as a reliable tracer of H<sub>2</sub> columns and not only in lower density (diffuse) clouds but also in denser high mass star formation regions. This is contrary to the previously mentioned expectations from chemical models for dense quiescent clouds (e.g., Herbst & Leung 1986 a,b) and suggests influences of shock chemistry (caused by bipolar outflows) in the denser star forming clouds (as was concluded already by Turner 1988, based upon his detailed analysis of the  $\approx 700$  MHz CH absorption line data).

The *Herschel* HIFI detections by Falgarone et al. (2010a) of the CH<sup>+</sup>(1–0), and <sup>13</sup>CH<sup>+</sup>(1–0), absorption lines at 835 and 830 GHz in the directions of the same star-formation regions also showing CH absorptions, confirmed the long standing problem that the observed CH<sup>+</sup> abundance versus H<sub>2</sub>  $\approx 5 \times 10^{-8}$ , i.e. similar to that of CH and several orders of magnitude higher than the predictions by UV-driven steady state PDR chemistry models. So-called turbulent dissipation models, where the activation energy ( $\approx 4600$  K), needed for the endothermic reaction C<sup>+</sup> + H<sub>2</sub> = CH<sup>+</sup> + H, is drawn from dissipation of turbulence, appear to provide the solution of this dilemma (TDR; Falgarone et al. 2010a; see Gerin et al. 2016 for a discussion and further references). In their *Herschel* HIFI observations of CH<sup>+</sup> toward the massive star-formation region DR 21 molecular cloud ridge – one of the most powerful molecular outflows seen in vibrationally excited H<sub>2</sub> – another CH<sup>+</sup> surprise appeared, in terms of a strong broad CH<sup>+</sup>(1–0) emission line from the cloud core, together with the expected deep absorption features from the DR 21 molecular ridge and foreground gas (Falgarone et al. 2010b). The broad emission was satisfactorily interpreted by means of a state-of-the-art C-shock model in dense, UV-illuminated gas (Falgarone et al. 2010b), while the absorptions were consistent with TDR modeling results (Falgarone et al. 2010a).

The importance of intense UV-illumination for the CH<sup>+</sup> formation in dense molecular cloud PDR surfaces became very clear from the *Herschel* observations of CH<sup>+</sup> in the Orion Bar (Nagy et al. 2013, 2017) and the mapping of CH<sup>+</sup> and CH in an extended region including Orion KL as well as the Orion Bar (Morris et al. 2016). In the Orion Bar the CH<sup>+</sup> ( $J = 1 - 0$  and  $2 - 1$ ) emission lines turned out to be markedly broader than other molecular lines ( $\Delta v \approx 5 \text{ km s}^{-1}$  vs  $\approx 3 \text{ km s}^{-1}$ , as observed by HIFI), and the strong higher energy lines observed by PACS (up to  $J = 6 - 5$  at an upper state energy of 838 K) and indicate a kinetic temperature of 500–1000 K. This very high rotational excitation of CH<sup>+</sup> together with the line broadening are clear signs of “formation pumping”, where the activation energy of 4600 K, required for the endothermic reaction C<sup>+</sup> + H<sub>2</sub> = CH<sup>+</sup> + H to take place, is supplied by vibrationally (and rotationally) excited H<sub>2</sub>, caused by the intense UV-illumination in the observed regions. The H<sub>2</sub> excited state excess energy here will cause the high rotational excitation of CH<sup>+</sup> as well as line broadening by addi-

tional translational CH<sup>+</sup> motion (as discussed in detail by Nagy et al. 2013 and theoretically modeled by Godard and Cernicharo 2013; see also Gerin et al. 2016 for discussions and references). In the Orion Bar the observed CH<sup>+</sup> population distribution leads to a column density 40 times larger than the “minimum” column density calculated from the CH<sup>+</sup>( $J = 1 - 0$ ) emission line, assuming a “reasonable” excitation temperature in the range 20 – 150 K, and hence an estimated CH<sup>+</sup> abundance larger than that of CH (Table 2 of Nagy et al. 2017). This CH<sup>+</sup> formation scenario is favored also for the extended Orion molecular cloud surface where (some) CH also may result from dielectronic recombination of CH<sup>+</sup> (Morris et al. 2016).